Using palladium and gold-palladium nanoparticles decorated with molybdenum oxide for versatile hydrogen peroxide electroproduction on graphene nanoribbons

Guilherme V. Fortunato[a,b*], *Leticia S. Bezerra*[b], *Eduardo S. F. Cardoso*[b], *Matheus S. Kronka*[a], *Alexsandro J. Santos*[a], *Anderson S. Greco*[c], *Jorge L. R. Júnior*[b], *Marcos R. V. Lanza*[a], *Gilberto Maia*[b*]

[a]São Carlos Institute of Chemistry, University of São Paulo, Avenida Trabalhador São-Carlense 400, São Carlos, SP 13566-590, Brazil

[b]Institute of Chemistry, Federal University of Mato Grosso do Sul; Av. Senador Filinto Muller, 1555; Campo Grande, MS 79074-460, Brazil

[c] Faculty of Exact Sciences and Technology, Federal University of Grande Dourados, Highway Dourados-Itahum, km 12, Dourados, MS 79804-970, Brazil

*Corresponding authors' e-mails:

g.fortunato@usp.br (G.V. Fortunato)

gilberto.maia@ufms.br (G. Maia)

ABSTRACT: Electrocatalytic production of H_2O_2 via 2-electron oxygen reduction reaction (ORR-2e$^-$) is regarded a highly promising decentralized and environmentally friendly mechanism for the production of this important chemical commodity. However, the underlying challenges related to the development of catalytic materials that contain zero or low content of noble metals and which are relatively more active, selective, and resistant for long-term use have become a huge obstacle for the electroproduction of H_2O_2 on commercial and industrial scale. The present study reports the synthesis and characterization of low metal-loaded (≤6.4 wt.%) catalysts and their efficiency in H_2O_2 electroproduction. The catalysts were constructed using gold-palladium molybdenum oxide ($AuPdMoO_x$) and palladium-molybdenum oxide ($PdMoO_x$) nanoparticles supported on graphene nanoribbons. Based on the application of a rotating ring-disk electrode, we conducted a thorough comparative analysis of the electrocatalytic performance of the catalysts in ORR under acidic and alkaline media. The proposed catalysts exhibited high catalytic activity (ca. 0.08 mA $g^{-1}_{\text{noble metal}}$ in acidic medium and ca. 6.6 mA $g^{-1}_{\text{noble metal}}$ in alkaline medium), good selectivity (over 80%), and improved long-term stability toward ORR-2e$^-$. The results obtained showed that the enhanced ORR activity presented by the catalysts, which occurred preferentially via 2-electron pathway, was promoted by a combination of factors including geometry, Pd content, interparticle distance, and site blocking effects, while the electrochemical stability of the catalysts may have been enhanced by the presence of MoO_x.

KEYWORDS: oxygen-reduction reaction, hydrogen peroxide production, graphene nanoribbon, gold-palladium alloy, molybdenum decoration.

1. Introduction

According to a recent report from the Global Market Insights Inc., the total worth of the market for hydrogen peroxide — listed as one of the 100 most important chemical compounds [1]— is estimated to exceed \$6.2 billion by 2026 [2]. The overall market demand for hydrogen peroxide is expected to be fueled by the chemical, paper and pulp industries, as well as by the increasingly growing demand for H_2O_2 in areas such as industrial water treatment for the end user (using H_2O_2 to remove impurities and reduce odors), among others [2,3]. Currently, approximately 95% of H_2O_2 is produced in large scale by very few industries based on the application of the conventional anthraquinone method using O_2 and H_2; the hydrogen peroxide produced by these industries is distributed to the consumers in a highly concentrated aqueous form [4,5]. As pointed out in the literature, for smaller scale and on-site consumption of hydrogen peroxide, where the compound is typically consumed in diluted conditions (< 10 wt.%), the use of decentralized or on-site H_2O_2 production methods have been found to contribute toward the reduction of costs and risks related to transport and storage [5,6]. As an efficient and eco-friendly alternative, the electrocatalytic production of H_2O_2 via oxygen reduction reaction (ORR) offers the possibility for the process to be conducted under ambient conditions and at varying rates using scalable plants, including on-site point of utilization [5–9].

As reported elsewhere, one requires the development of highly stable, active, selective, and economically accessible catalysts to make the production of H_2O_2 by ORR on industrial scale commercially viable [10,11]. In acidic environments, catalysts constructed using noble metals are found to be very active and are expected to resist the severe reaction conditions in this atmosphere [12–14]. Metals, such as gold (Au), mercury (Hg), and silver (Ag), which do not strongly interact with O_2 typically exhibit high selectivity toward the reduction of O_2 to H_2O_2 ($O_2 + 2H^+ + 2e^- \rightarrow H_2O_2$)

at slow rate where high overpotentials are required (potential in relation to $E^0_{O2/H2O2} = 0.695$ V *vs* RHE) [15–17]; in alkaline medium, these same metals may exhibit improved ORR activity and selectivity toward oxygen reduction to hydroxyl (OH^-) in 4-electron pathway ($O_2 + 2H_2O + 4e^- \rightarrow 4OH^-$) [18–23]. In contrast, active noble metals, such as platinum (Pt) and palladium (Pd), which exhibit a strong interaction with O_2 and tend to reduce O_2 to H_2O in a 4-electron pathway in both acidic and alkaline media [17,24,25], can be used in combination with less active metals (nanoalloys) to produce highly active catalysts that are selective for H_2O_2 production [6,7]. By geometric (or ensemble) effect, the presence of single Pt or Pd atoms (active metal) surrounded by less active atoms on the surface of the electrocatalyst can help boost its selectivity; these active isolated atoms are sterically prevented from breaking the O−O bond, as demonstrated in the literature via the application of Au-Pd [13,14,26,27], Hg-Pt [6], Pt-Ag [28] and Pd-Hg [7]. Through DFT calculations on PdAu(111) surfaces, previous studies have demonstrated the need to have large Pd ensembles for the O_2 dissociation barrier to be markedly reduced in comparison with the pure Au surface. Few Pd atoms (1 or 2) in the ensemble in Au(111) are found to present an elevated O_2 dissociation barrier [29]. Also, it has been suggested that the introduction of dopant metals with appropriate electronegativity in Pd or PdAu surfaces may lead to changes in the valence electrons of Pd-shell atoms, causing impacts on catalytic activity and selectivity [30]. With regard to Pt-Ag, reports in the literature have shown that the presence of Ag combined with Pt contributes to the selective activation of ORR via two-electron pathway due to the inhibition of O_2 dissociation by the prevention of H_2O_2 adsorption and decomposition [28]. In a study conducted by Rossmeisl et al. [6,7], the authors showed that the presence of Hg atoms (catalytically inactive) resulted in the isolation of active sites of metals like Pt and Pd, and this led to high selectivity for H_2O_2 production due to the optimal binding energy of these metals to HOO^* (adsorbed intermediate). Similarly, the breakage of the O−O bond can be suppressed in Pt or Pd bulk catalyst if the surface of the catalyst is poisoned with impurities [24,31] or strategically covered by carbon layers [32] or ions [33,34].

For applications in alkaline environments, the most selective materials for H_2O_2 electrocatalytic production are metal-free carbon-based materials such as carbon black, aerogel carbon, carbon nanotubes, and graphene functionalized with oxygenated groups coordinated or not with nitrogenated groups [28,35–37]. More recently, studies published in the literature have employed distinct functionalized carbon materials as catalysts for the production of H_2O_2 with high selectivity in acidic solution [36,38–40]. However, these studies were found to employ relatively higher overpotentials [35,37,41] for ORR in comparison with metal-based electrocatalysts in both acidic and alkaline media [10,35,37,41,42]; in addition, the studies also failed to address some underlying problems related to the electrochemical stability of the proposed techniques.

Despite the great advances made in the construction of suitable materials for the electrocatalytic production of H_2O_2, further studies are still needed to be conducted with a view to developing highly efficient and selective electrocatalysts that are either free of noble metals or contain low quantities of noble metals and which are capable of maintaining the high catalytic activity of the electrocatalyst even after a long period of use. In the present work, we sought to synthesize highly active nanocatalysts (with ORR performance equal or superior to state-of-the-art catalysts, which will be shown later) with improved selectivity (> 80 %) and long-term stability toward H_2O_2 production using low contents ($\leq$6.4 wt.%) of Pd and Au-Pd supported on graphene nanoribbons (GNR) and decorated with MoO_x based on the application of the hydrothermal method. The synthesized materials were characterized by micrographic, spectroscopic and electrochemical techniques, while the ORR activity, selectivity, and long-term electrochemical stability were carefully examined by the rotating ring-disk electrode (RRDE) technique using different supporting electrolytes ($HClO_4$, H_2SO_4, and KOH solutions).

2. Experimental details

2.1. Chemicals and instruments

All the chemicals (salts and precursor solutions) employed in the experiments were acquired commercially and were used as received or in diluted form. The following compounds were used in the experiments: $HAuCl_4 \cdot 3H_2O$, $Na_2MoO_4 \cdot 2H_2O$ (>99%, both obtained from Sigma-Aldrich), $PdCl_2$ (>99%, from Sigma-Aldrich), KOH, ascorbic acid (>99%, all acquired from Vetec), Pluronic F-127 (>99%, from Aldrich), $HClO_4$ (70%, obtained from Sigma-Aldrich), and H_2SO_4 (98%, acquired from Vetec). Multi-walled carbon nanotubes employed in the experiments were based on the following specifications: 10 ± 1 nm o.d. × 4.5 ± 0.5 nm i.d. × 3−6 µm-long, 6−8 tube walls (acquired from Aldrich).

All the electrochemical measurements were performed in a three-electrode glass cell with a rotating ring-disk working electrode (RRDE) which consisted of a glassy carbon (GC) disk and a Pt rotating ring assembly, with geometric area of 0.196 and 0.11 cm^2, respectively. The collection efficiency of the ring electrode (*N*) was 0.26 - as provided by the manufacturer (Pine Research Instrumentation). A graphite rod and a reversible hydrogen electrode were used as counter electrode and reference electrode, respectively.

2.2. Electrode preparation

The GC disk working electrode was polished with alumina slurries (1 and 0.05 mm) and was finally cleaned by sonication in ultrapure water, acetone, and ultrapure water for 5 min in each solvent. Subsequently, the GC disk electrode was treated electrochemically through the application of 10 voltammetric cycles at scan rate of 50 mV s^{-1} and potential range of 0.05−1.2 V. The Pt ring was treated using 200 voltammetric cycles at scan rate of 900 mV s^{-1} and potential range of 0.05−1.2 V. A uniform thin film with an area loading of 152.7 mg cm^{-2} was generated subsequently by drop-casting 30 mL of aqueous solution of the catalysts at 1 mg mL^{-1} on the GC disk surface; the solution was allowed to dry at room temperature. The modified electrodes were placed in an electrochemical cell containing 0.1 M $HClO_4$, 0.5 M H_2SO_4, or 0.1 KOH solution, which was then saturated with N_2 (5.0 purity) or O_2 (4.0 purity) (both N_2 and O_2 were acquired from White Martins).

2.3. Physical-chemical characterization methods

To perform the transmission electron microscopy (TEM) and scanning-TEM (STEM) analyses, the catalyst dispersion (previously prepared from the fresh catalyst or film carefully washed and collected from the electrode surface) was dropped on a TEM grid which consisted of a lacey carbon film supported on a copper grid (300-mesh, Electron Microscopy Sciences). The TEM and STEM analyses were performed using JEOL JEM 2200F and FEI TECNAI G² F20 HRTEM microscopes - both microscopes with electron beam of 200 kV. For the energy-dispersive X-ray spectroscopy (EDS) analysis, aqueous solutions of the catalysts were dripped onto fluorine-doped tin oxide (FTO, Flexi Tec Eletrônica Orgânica) plates (1.0 cm × 1.0 cm × 0.1 cm) which were subjected to EDS measurements using Thermo Noran System Six equipment. The EDS analysis was performed in order to microanalyze the proportions of Pd, Au, and Mo in the catalysts samples. The atomic compositions reported represent the average of three measurements of the same sample. The thermogravimetric characterization of the GNRs, the Pluronic F-127, and the metals/GNRs was performed with the aid of a Shimadzu TGA-50 thermogravimetric analyzer, operated under a Synthetic Air 5.0 FID gas flow (50 mL min^{-1}) at temperatures ranging from ambient to 700 °C and a heating rate of 10 °C min^{-1}, using ceramic alumina crucibles. The determination of the loading of each metal present in the samples was performed by the combination of thermogravimetry and EDS techniques [43]. In addition, the exact composition of Au, Pd and Mo in GNR-based materials was determined by inductively coupled plasma optical emission spectrometry (ICP OES) using a Thermo Scientific iCAP 6300 spectrometer (Thermo Fisher Scientific®, Bremen, Germany) with a high performance CID86 chip detector. The experimental details related to the ICP OES analyses can be found in the Supplementary Information.

The structural characterization of the metals/GNRs was performed by X-ray diffraction analysis (XRD) using a Shimadzu XRD-600 diffractometer or a Bruker D8 Advance ECO diffractometer, both operated at the potential of 40 kV, using current density of 40 mA and Cu-Kα radiation (λ = 1.5418 Å). The XRD analyses were carried out using catalyst powder for the non-electrochemically stabilized catalysts and thin films prepared on HCP030N-type carbon paper for the electrochemically stabilized catalysts. The diffractograms were obtained using a scan rate of 0.02° s^{-1} in 2θ, with an internal reference made up of silicon powder.

The X-ray photoelectron spectroscopy (XPS) analyses were performed with the aid of OMICRON (CHA - Concentric Hemispherical Analyser) or Scientia Omicron ESCA spectrometers, using Al/Ka radiation (1486.6 eV) and anode operated at the potential of 15 kV, with current density of 15 mA and power of 225 W. The survey spectra were recorded using pass energy of 50 eV and pitch of 1 eV, while the higher resolution spectra were recorded using pass energy of 10 eV and pitch of 0.1 eV. The XPS samples from the non-electrochemically and electrochemically stabilized catalysts were deposited on copper tape in a molybdenum carrier and transferred to the pre-chamber under inert atmosphere. The inelastic noise from the high-resolution spectra for Au 4f, Pd 3d, Mo 3d, C1s, N 1s, and O1s was subtracted using the Shirley's method. The deconvolution of the narrow spectra was done using the Casa XPS® software based on a Voigt type function with Gaussian (70%) and Lorentzian (30%) combinations.

2.4. Apparatus and measurements

Cyclic voltammetry (CV) and linear sweep voltammetry (LSV) analyses were performed using AFP2 WaveDrive 20 bipotentiostat/galvanostat coupled to an AFMSRCE modulated speed rotator (acquired from Pine Research Instrumentation).

A PGSTAT128N potentiostat/galvanostat (Autolab) equipped with FRA2.X module was used to perform the impedance assays; the assays were performed at open circuit potential via the application of an average potential of 0.80 V *vs.* RHE in N_2-saturated supporting electrolyte with potential perturbation of 25 mV and frequency range of 10 mHz to 100 kHz. Each linear sweep voltammetry curve was compensated for ohmic drop resistance measured and determined from the fitted high-frequency intercept measured by the EIS technique. The values obtained for ohmic drop resistance (on average) in 0.1 M $HClO_4$, 0.5 H_2SO_5, and 0.1 KOH were 33, 22, and 29 Ω, respectively.

The long-term electrochemical stability of the synthesized catalysts was evaluated using accelerated stress testing (AST) which consisted of the application of 8,000 voltammetric cycles in the potential range of 0.4 - 1.0 V *vs.* RHE (AST) at room temperature, using O_2-saturated solution and scan rate of 200 mV s^{-1}.

2.5. Estimation of selectivity toward H_2O_2 production (S_{H2O2}) and number of electrons transferred (n) in the process

The potential-dependent S_{H2O2} and the number of electrons transferred per O_2 molecule (*n)* were calculated using the data obtained from the RRDE-based analysis. The S_{H2O2} values were calculated according to Equation 1 below [44,45]:

$$S_{H_2O_2} = \frac{2I_\mathrm{r}/N}{I_\mathrm{d} + I_\mathrm{r}/N} x\ 100\% \qquad (1)$$

where I_d is the measured disk current, I_r is the ring current, which is given by the H_2O_2 oxidation, and N is the efficiency of collection for the ring electrode ($N = 0.26$). The n values were calculated using Equation 2 below [44,45]:

$$n = \frac{4I_\mathrm{d}}{I_\mathrm{d}+\frac{I_\mathrm{r}}{N}} \qquad (2)$$

2.6. Synthesis of graphene nanoribbons (GNR)

The synthesis of GNRs using multi-walled carbon nanotubes (MWCNTs) and the analysis of the surface and physical properties of the GNRs can be found in detail elsewhere [46]. Briefly, MWCNTs were dispersed in concentrated H_2SO_4 solution, mixed with $K_2S_2O_8$ and P_2O_5, and subjected to heating. After washing, the pre-oxidized material was re-oxidized by adding H_2SO_4, $NaNO_3$, and $KMNO_4$. Following the re-oxidation reaction, the material was mixed with H_2O_2, and this led to the production of graphene oxide nanoribbons (GONRs). GNRs were formed after the immersion of the GONRs in hydrazine sulfate and NH_3OH.

2.7. Synthesis of $AuPdMoO_x$ *on GNRs*

The synthesis of $AuPdMoO_x$ on GNRs was performed as follows: initially, an amount of 16 mg of GNRs was solubilized with 46 µL of 0.1 M $HAuCl_4$ aqueous solution, 0.55 mg of $PdCl_2$, and 4.24 mg of Pluronic F-127 (used as structure-directing agent of metallic nanoparticles [47]) in 10 mL Milli-Q water by ultra-sonication. A relatively low amount of surfactant (ca. 3:1 in relation to the metal mass) was chosen tentatively in order to restrict the size, shape and dispersibility of the nanoparticles, as well as to avoid the need for taking additional steps for the cleaning of the formed nanoparticles. After solubilization, the mixture was heated to boiling point using a hot plate, under magnetic stirring. Subsequently, a solution of 800 µL of ascorbic acid (AA) (17.9 mg mL^{-1} in water) was quickly added to the mixture; 5 minutes later, an amount of 60 µL of Na_2MoO_4 solution (4.2 mg mL^{-1} in water) was added, and immediately thereafter, another amount of 200 µL of AA solution was added to the mixture. The mixture was kept boiling for 5 minutes. After that, the heating was stopped, and the mixture was kept under stirring for 2 hours so that the $AuPdMoO_x$ nanoparticles were supported on the surface of the GNRs. The same procedure and quantities (Table S1) were employed for the preparation of the other catalysts; however, the catalysts containing less metal/metals (mono and bimetallic structures) were produced without the application of the quantities and the respective synthesis procedure related to the metal (or metals) absent in these catalysts. All the nanocomposites formed were cooled to room temperature and centrifuged with Milli-Q water (10 times) to remove the surfactant and any reactants that did not undergo reaction in the mixture; the material was finally left to dry overnight in an oven at 40 °C.

3. Results and discussion

3.1. Characterization of the Material

Figure 1a illustrates the synthesis procedures employed in obtaining the $AuPdMoO_x$ nanoparticles on graphene nanoribbons (GNRs). The first step, which involved the reduction of Au^{3+} and Pd^{2+}ions, led to the formation of Au-Pd nanoparticles with shapes varying between tetrahedral, octahedral, decahedral and icosahedral structures, and sizes ranging from 10 to 100 nm (Fig. S1). The second step, which involved the addition of molybdate ions to the AuPd nanoparticle system, led to the production of $AuPdMoO_x$ nanoparticles. As can be noted in Figure 1b, the TEM and the black-field (BF) and dark-field (DF)-STEM images (see Fig. S2) clearly show the wide distribution of the particles with different shapes on the GNRs. The diversity observed in the shapes of the particles can be attributed to the presence of different crystalline phases [48]. Figure 1b and the histogram of the particle size distribution (inset - Fig. 1b) display particle sizes ranging from 10 to 90 nm, with more predominant sizes of approximately 18 nm.

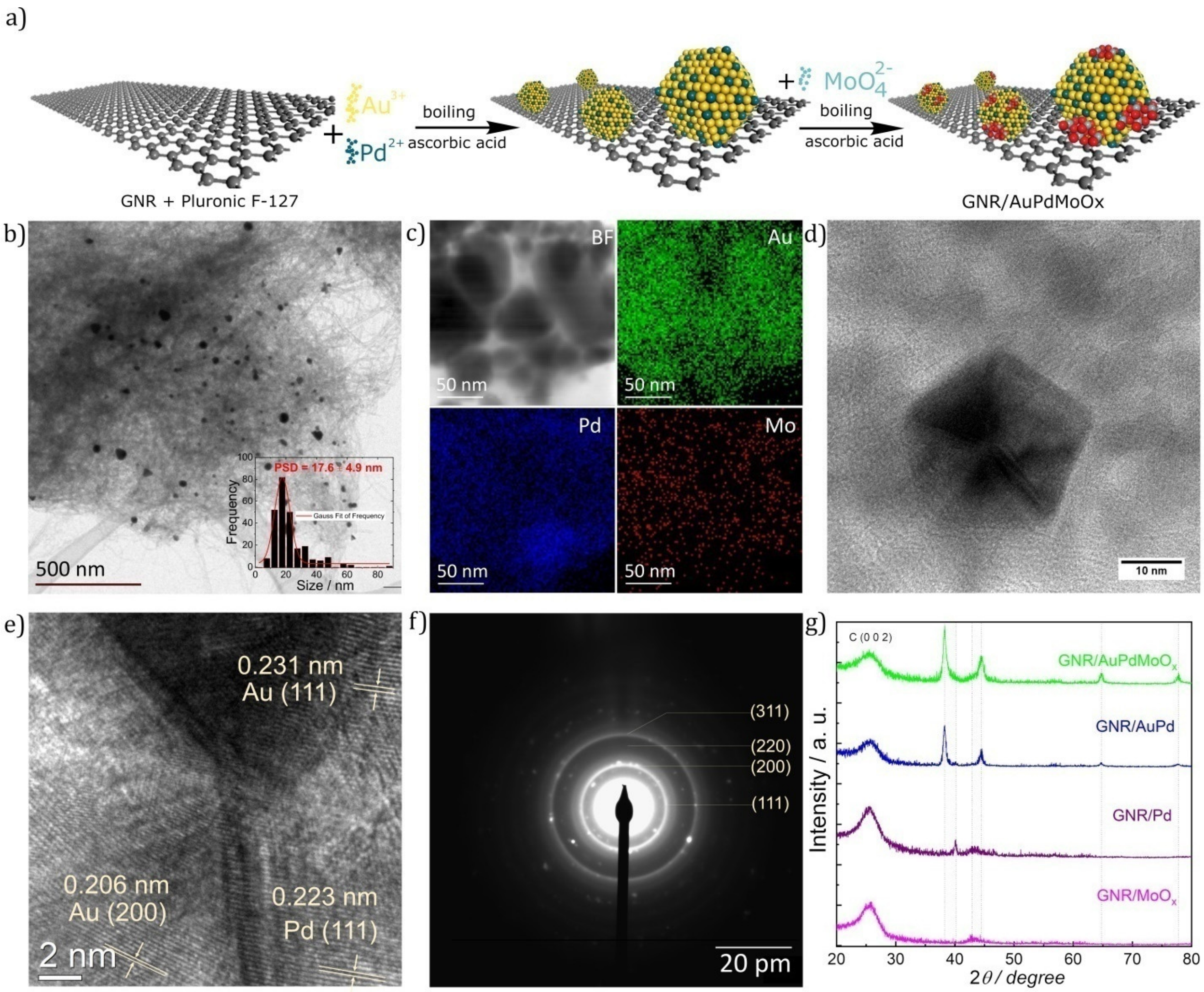

Figure 1. (a) Schematic representation of the synthesis procedures employed in obtaining the GNR/AuPdMoO$_x$ catalyst. (b) TEM image and (inset) histogram related to the particle size distribution. (c) Elemental EDS-mapping, (d,e) HR-TEM, and (f) electron diffraction pattern images for the GNR/AuPdMoO$_x$ catalyst. (g) XRD patterns obtained for the GNR/Au-Pd/MoO$_x$, GNR/Au-Pd, GNR/Pd, and GNR/MoO$_x$ samples.

The elemental EDS-mapping images obtained for the non-electrochemically stabilized GNR/AuPdMoO$_x$ catalyst (Fig. 1c) show that the three metals have been widely distributed on the nanoparticles and they have not produced core-shell structures. Although the results obtained from the elemental mapping also suggest the enrichment of Pd to a certain extent, these results point to the alloying characteristics of the AuPd structures, where one notices the occurrence of a greater distribution of the molybdenum oxide and a larger exposure of Au on the surface of the particles. The EDS line scan analysis (Fig. S3) also indicates the occurrence of a larger exposure of Au along with a broad distribution of Mo on the surface of the nanoparticles. Figures 1d-1f show the high-resolution TEM (HR-TEM) and selected area electron diffraction (SAED) images which provide us with further morphological and crystalline characteristics of the non-electrochemically stabilized GNR/AuPdMoO$_x$ catalyst. The TEM images (c.f. Figs. 1 and S2) suggest that the nanoparticles grow mainly on the edges of the nanoribbons probably due to the high number of functional groups (O and N groups) present in GNRs which act as anchorage points for the nucleation of the metals [42]. The HR-TEM images point to the polycrystallinity of AuPdMoO$_x$ nanoparticles; the images mostly show the presence of lattice fringes with distances of 0.206 and 0.231 nm, which are typically related to the planes (200) and (111) and correspond to the face-centered cubic structure *(fcc)* of Au [49,50]. Although to a relatively lesser extent, the HR-TEM images also show the presence of lattice fringes with distance of 0.223 nm which correspond to the plane (111) and are related to the cubic structure of Pd (JCPDS 894897). The SAED pattern obtained for the GNR/AuPdMoO$_x$ catalyst also indicates the face-centered cubic crystalline characteristic of the nanoparticles. Figure S4 shows the TEM images obtained for the GNR/AuPdMoO$_x$ catalyst after it was subjected to electrochemical long-term stability test (this is identified as electrochemically stabilized GNR/AuPdMoO$_x$ catalyst). The TEM image obtained for the electrochemically stabilized GNR/AuPdMoO$_x$ sample shows that there were no changes in the shape, size and crystallinity of the nanoparticles in comparison with the non-electrochemically stabilized GNR/AuPdMoO$_x$ sample; this result points to the high long-term stability of the structure of the electrochemically stabilized GNR/AuPdMoO$_x$ catalyst.

Figures 2 and S5 show the TEM, HR-TEM, STEM, and SAED images, as well as the EDS line scan results obtained for the nanoparticulate system produced without the presence of Au – denominated the non-electrochemically stabilized GNR/PdMoO$_x$ catalyst. Looking at the TEM (Fig 2a) and STEM (Fig. S5) images, one can observe the presence of small spherically shaped particles (~5 nm, on average) widely distributed on the GNR. The HR-TEM image points to the crystalline characteristic of the PdMoO$_x$ nanoparticles; the image shows the presence of lattice fringes with distance of 0.223 nm (predominantly) which correspond to the plane (111) and are attributed to the *fcc* structure of Pd (JCPDS 894897). Although to a lesser extent, the HR-TEM image (Fig. 2b,c) also shows the presence of lattice fringes with distance of 0.240 nm which correspond to the plane (020) and are attributed to monoclinic MoO$_2$ [51,52]. The SAED pattern obtained for the GNR/PdMoO$_x$ catalyst (Fig. 2d) also points to the *fcc* crystalline characteristic of the nanoparticles. The EDS line scan analysis (Fig. 2e,f) shows that Pd and Mo were equally distributed in the formation of the particles. Figure S6 shows the TEM and HR-TEM results obtained for the non-electrochemically stabilized GNR/Au, GNR/Pd, and GNR/MoO$_x$ catalysts; these catalysts were synthesized for comparison purposes. The TEM image in Figure S6a-b shows that the GNR/Au sample presented crystalline nanoparticles with shape and size similar to GNR/AuPd and GNR/AuPdMoO$_x$ (c.f. Figs 1, 2, S1 and S6), while the GNR/Pd sample (S6b,c) exhibited truncated octahedral and icosahedral-shaped particles which were found to be slightly deformed. The TEM image obtained for the GNR/MoO$_x$ catalyst (S6e) shows the presence of small spherical nanoparticles (~10 nm on average) which tended to form highly porous agglomerates. The HR-TEM image (S6f) obtained shows the presence of lattice fringes with distances of 0.342 and 0.240 nm which correspond to the planes (110) and (020) and are attributed to monoclinic MoO_2, and lattice fringes with distance of 0.266 nm which correspond to the plane (111) and are attributed to orthorhombic MoO_3[51,52]; these results indicate the formation of a combination of molybdenum oxides (MoOx). It is relevant to point out that, for all the catalysts produced, a relatively low amount of surfactant (ca. 3:1 in relation to the metal mass) was used tentatively to restrict the size, shape and dispersibility of the nanoparticles. The results obtained from the electron microscopic analysis (Fig. S7 and S8) clearly show that in the absence of Pluronic F-127, despite their smaller sizes, a much larger variety of particle size and shape are obtained, as well as highly non-uniform distributions.

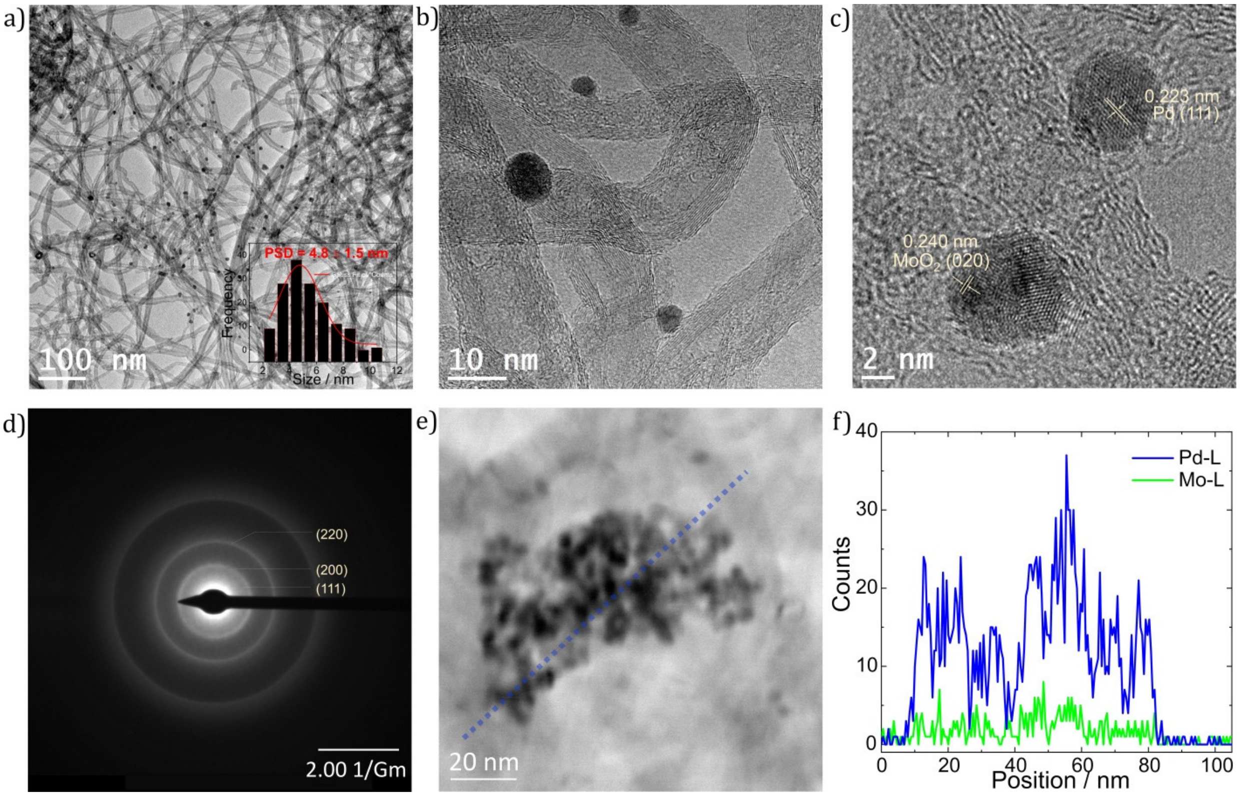

Figure 2. (a) TEM image and (inset) histogram related to the particle size distribution; (b,c) HR-TEM; (d) electron diffraction pattern images for the GNR/PdMoO$_x$ catalyst; (e,f) EDS line scan analysis for the GNR/PdMoO$_x$ catalyst.

The crystallinity of the catalysts samples was further investigated by XRD; the results obtained are shown in Figures 1f and S9. With regard to the XRD patterns obtained for the GNR/AuPd and GNR/AuPdMoO$_x$ samples, one can observe the presence of four sharp diffraction peaks that correspond to Au (111), (200), (220), and (311) planes at 2θ values of 38.3°, 44.5° 64.8°, and 77.7° (JCPDS 040784); these results are in line with the SAED patterns (c.f. Figures 1 and S1). A careful inspection of the XRD patterns obtained for the GNR/AuPd, GNR/AuPdMoO$_x$ and GNR/Pd samples shows the presence of less intense peaks which correspond to (111), (200), (220) planes at 2θ values of 40.1°, 46.6°, 68.0°; these peaks are typically associated with the face-centered cubic structure of Pd (JCPDS 894897). It is worth noting, however, that the catalysts samples containing molybdenum (GNR/AuPdMoO$_x$ and GNR/MoO$_x$) did not show diffraction peaks related to the crystalline structures of molybdenum oxide; this can be attributed to the low amount of the metal in the samples.

Thermogravimetric analysis (TGA) was used to evaluate the thermal stability and metal loading of the synthesized catalysts; the responses obtained are shown in Figure S10. For all the catalysts samples investigated, a slight mass loss was observed at 220 ºC. This mass loss was attributed to the presence of the residues of Pluronic F-127 surfactant, which was used as a nanostructuring agent for the growth and dispersibility of the particles [43,49,53]; the surfactant residues remained in the catalysts even after several washing cycles by centrifugation. The GNR support was found to have been completely burned at 570 ºC, and the only thing left (unburned) was the metal mass (probably in the oxidized form) which remained stable even at higher temperatures; these observations are in agreement with the results obtained in previous studies reported in the literature [49,54]. The thermogravimetric responses showed that the metal loading employed for all the catalysts was low; the highest loading was 6.4 wt.%. Table S1 shows the mass and atomic percentage values for Au, Pd, Mo, and C present in the catalyst samples; these values were initially determined by the combination of TGA and EDS analyses, and were later confirmed by ICP OES assays (c.f. Table S3). The GNR/AuPdMoO$_x$ catalyst exhibited a total metal loading of 5.6 wt.% with a ratio of ~10:3:1 between Au, Pd, and Mo, respectively. Alloys constituted by Au and Pd with Au enrichment are found to be highly active and selective toward 2-electron transfer ORR [16,26]. The GNR/PdMoO$_x$ catalyst exhibited a metal loading of 2.2 wt.% with a ratio of ~6:1 between Pd and Mo, respectively. Additional information on the initial and final percentage values and the ratio between the metals and carbon can be found in Tables S1 and S3.

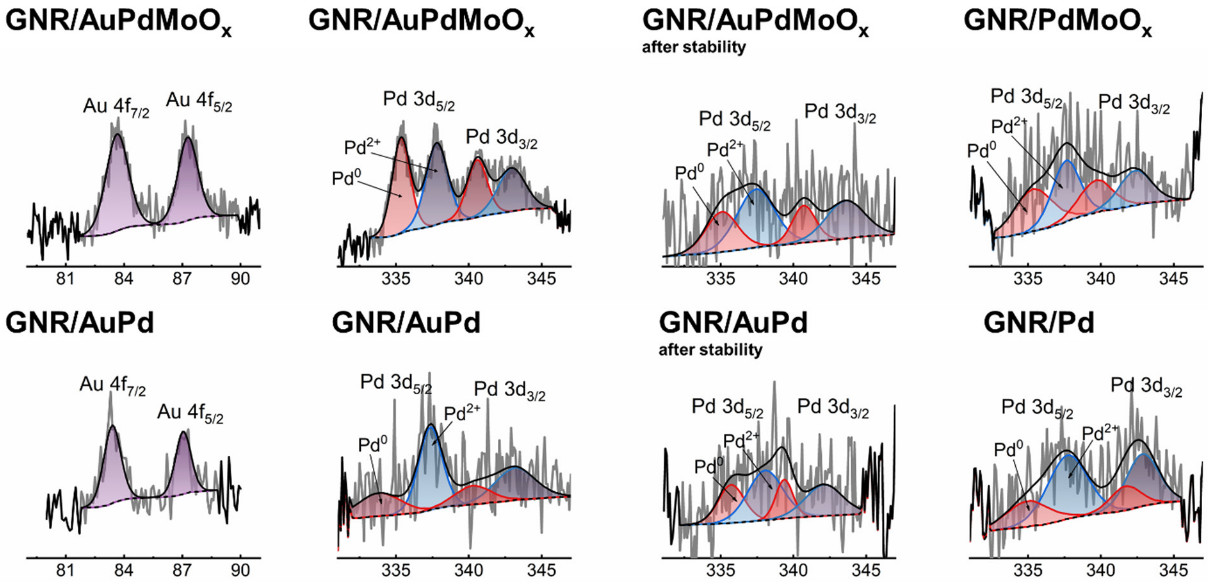

Figure 3. Narrow-scan XPS spectra of Pd 3d and Au 4f regions obtained for the GNR/Metal catalysts.

Figure S11 shows the XPS survey spectra obtained for the different catalysts (before and after stability test) synthesized in this work; as can be noted, the figure displays only the predominant peaks related to C 1s and O 1s at 284 and 532 eV (on average), respectively, with average % mass contents of 88 and 12, respectively (Table S4). The appearance of only two peaks suggests the presence of very small amount of metals in the synthesized nanocomposites.

To examine the presence and the chemical state of the metals in the catalysts, narrow-scan XPS spectra of Au 4f, Pd 3d, and Mo 3d regions were recorded, as well as the narrow-spectra of C 1s, O 1s, and N 1s regions (Figures 3 and S12). The presence of Au was confirmed by the identification of two peaks (with % content ratio close to 4/3 between the peaks), attributed to $Au^0 4f_{7/2}$ and Au^0 $4f_{5/2}$ at 83.4 and 87.0 eV, respectively, [55–57] (c.f. Table S5 and Figure 3) for the non-electrochemically stabilized GNR/AuPd catalyst. Wang et al. [55] suggest that the shift of the position of the $Au^0 4f_{7/2}$ and Au^0 $4f_{5/2}$ peaks to lower binding energies (eV) in comparison with metallic Au, which typically presents values of 84 and 87.7 eV, [58] can be understood as a consequence of the charge transfer from Pd to Au, since Au is more electronegative than Pd [59–61]. When the GNR/AuPd catalyst is decorated with MoO_x (GNR/AuPdMoO_x), the $Au^0 4f_{7/2}$ and Au^0 $4f_{5/2}$ peaks are found to be visible, though with a slight shift to binding energies that are 0.2 eV higher (Table S5 and Figure 3). This shift can be linked to the oxidation of the alloy due to the presence of MoO_x, even though Pd is more electronegative than Mo. Unfortunately, the signals of the Au 4f energy level were not detected for the electrochemically stabilized GNR/AuPd and GNR/AuPdMoO_x catalysts.

The presence of Pd was confirmed by the identification of two couples of peaks attributed to $Pd^0 3d_{5/2}$ and $Pd^{2+} 3d_{5/2}$ and $Pd^0 3d_{3/2}$ and $Pd^{2+} 3d_{3/2}$ at 335, 337.7, 341.7, and 342.8 eV, respectively [33,42,49,55–57] (Table S5 and Figure 3) for the non-electrochemically stabilized GNR/Pd catalyst with spin-orbital separation of 5.1 eV between the $Pd^{2+}3d_{5/2}$ and $Pd^{2+}3d_{3/2}$ (these values are in agreement with the values reported in the literature [56,62]) and content ratio of 70% for PdO. Compared to the non-electrochemically stabilized GNR/Pd catalyst, when the Pd surface is decorated with MoO_x (non-electrochemically stabilized GNR/PdMoO$_x$ catalyst), one notices a decrease in % content of PdO from 70% to 51%; this outcome is seen to be more relevant than the displacement (in eV) observed in the position of the peaks (Table S5 and Figure 3) – essentially, the result shows that MoO_x reduces the oxidation of Pd.

For the non-electrochemically stabilized GNR/AuPd catalyst, the Pd-Au alloy promoted the displacement of $Pd^{0}3d_{5/2}$ and $Pd^{0}3d_{3/2}$ peaks to relatively lower binding energies (eV), with an average value of 1.3 eV, compared to the non-electrochemically stabilized GNR/Pd catalyst (Table S5 and Figure 3); this behavior is attributed to the charge transfer from Pd to Au, since Au is more electronegative than Pd [59–61,63]. The % content of PdO (65.9%) is close to the value observed for the non-electrochemically stabilized GNR/Pd catalyst (Table S5 and Figure 3). When the surface of the AuPd alloy (non-electrochemically stabilized GNR/AuPdMoO$_x$ catalyst) is decorated with MoO_x, the positions of the $Pd^{0}3d_{5/2}$, $Pd^{2+}\,3d_{5/2}$, and $Pd^{0}3d_{3/2}$ peaks are displaced to higher binding energies (eV) in comparison with what is observed for the non-electrochemically stabilized GNR/AuPd catalyst (Table S5 and Figure 3). In addition, the decoration of the AuPd alloy with MoO_x leads to a decrease in % content of PdO from 65.9% to 50.7%; this outcome is similar to what is observed for the non-electrochemically stabilized GNR/PdMoO$_x$ catalyst in comparison with the non-electrochemically stabilized GNR/Pd catalyst (Table S5 and Figure 3). This result shows that the presence of MoO_x leads to a reduction in the oxidation of Pd in AuPd alloy. Interestingly, after the stability test, the electrochemically stabilized GNR/AuPdMoO$_x$ catalyst presented an increase in % content of PdO (63%) in comparison with the non-electrochemically stabilized GNR/AuPdMoO$_x$ catalyst (Table S5 and Figure 3). There was also a small decrease in the % content of PdO (63) for the electrochemically stabilized GNR/AuPd catalyst (after stability test)) compared to the non-electrochemically stabilized GNR/AuPd catalyst – which recorded PdO % content of 65.9% (Table S5 and Figure 3).

Unfortunately, we were unable to identify the presence of Mo through the narrow-scan XPS spectra (see the examples for GNR/AuPdMoO$_x$, GNR/MoO$_x$ and GNR/PdMoO$_x$ in Figure S12) due to the extremely low mass of this element in the samples and the low XPS Mo signal to noise. A detailed discussion of the results obtained for the narrow-scan XPS spectra of C 1s and O 1s regions can be found in the SI.

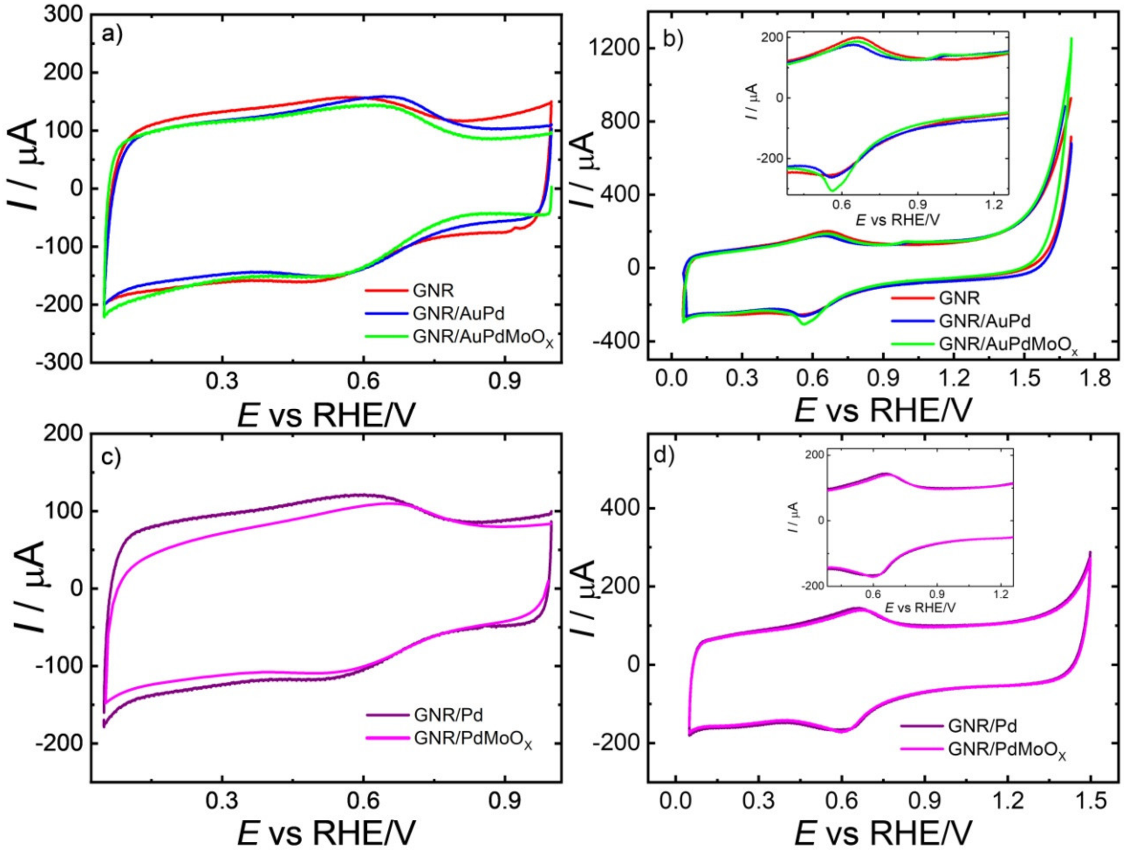

Figure 4. Cyclic voltammograms for GC electrodes modified with GNR/Metals catalysts in N$_2$-

saturated 0.1 M $HClO_4$ in the potential range of (a,c) 0.05–1.0 V and (b,d) 0.05–1.5 (or 1.7) V, with scan rate of 50 mV s^{-1}, starting at 1.0 V or at 1.7 V *vs.* RHE.

The synthesized catalysts were characterized by cyclic voltammetry using N_2-saturated 0.1 M $HClO_4$, as shown in Figures 4 and S13. The GNR modified electrode exhibited capacitive behavior with double layer charging and discharging currents, in addition to redox peaks around 0.6 V *vs.* RHE related to the presence of quinone groups on the GNR surface (Fig. 4a-b) [54,64]. In general, all the GNR/Metals nanocomposites exhibited electrochemical behavior very similar to that of bare GNR with only capacitive currents. In addition, for the catalysts containing Pd, the typical peaks related to the formation/reduction of PdO_x were not observed in both potential ranges, starting at 1.0, 1.5, or even at 1.7 V *vs.* RHE. This behavior can be attributed to the low content of Pd (≤ 2.6 wt.%, c.f. Tables S1 and S3) with the wide dispersion of the small particles (high interparticle distance); similar results have been found in previous studies reported in the literature for catalysts containing low contents of Pd [33,42]. Surprisingly, after a careful inspection of the CVs starting at 1.7 V, two small peaks which are not well defined were observed at ~1.0 and 0.7 V *vs.* RHE for the catalysts containing Au-Pd alloy (Fig. 4b); these peaks can be related to the formation/reduction of Au surface oxides [14,16,26]. Furthermore, a careful inspection of the voltammetric curves shows (in general) the occurrence of a slight decrease in the currents when the PGMs and MoO_x are supported on GNR surface (Figure 4); this indicates that the construction of the modified catalysts leads to a slight reduction in the GNR surface area. This observation reinforces the importance of the presence of very small amount of PGMs and MoO_x on GNRs (instead of being attributed to the GNR surface area effect) in the improvement of the catalytic activity and selectivity for H_2O_2 production through the application of the modified catalysts.

3.2. Evaluation of the electrocatalytic activity toward ORR

The ORR activity and selectivity of the synthesized catalysts were investigated by linear sweep voltammetry (LSV) using RRDE configuration in O_2-saturated 0.1 M $HClO_4$, as shown in Figures 5 and S14-16. While the LSV analysis for the catalyst-containing disk electrode was performed in the potential window between 0.05 and 1.0 V *vs.* RHE, the potential for the bare Pt ring electrode was kept at 1.2 V *vs.* RHE (potential favorable for H_2O_2 oxidation) in order to detect whether H_2O_2 was generated during the ORR [42]. Based on the disk and ring curves, one can obtain valuable information regarding the selectivity toward H_2O_2 production (S_{H2O2}) relative to the applied potential and the number of electrons transferred (n) in the course of the ORR. The S_{H2O2} and n were estimated from the disk current (i_d), ring currents (i_r), and the collection efficiency of the system (N) using equations (1) and (2).

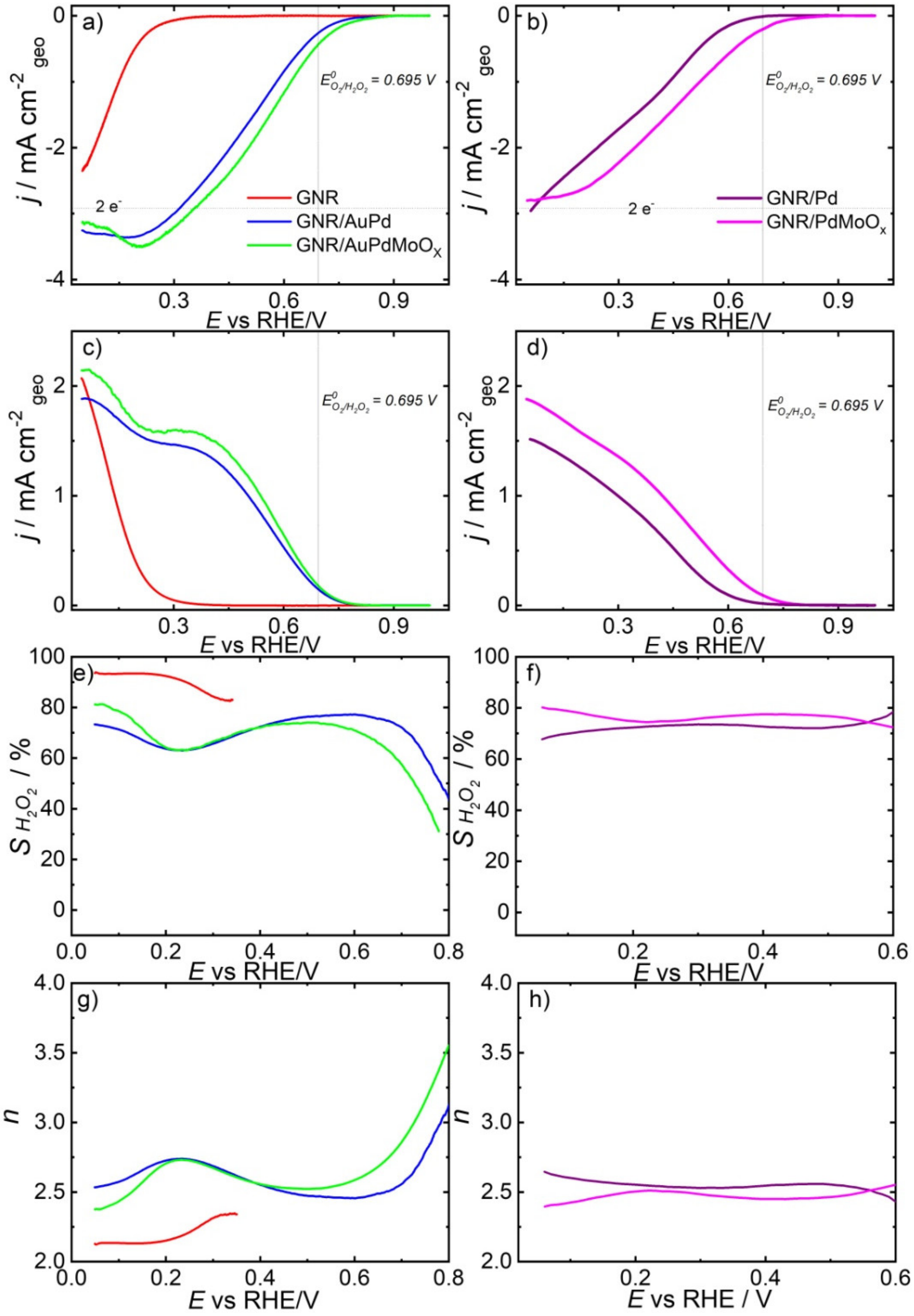

Figure 5. Results obtained from the linear sweep analysis conducted using RRDE for GC modified with GNR and GNR/Metals catalyst employed in O_2-saturated 0.1 M $HClO_4$ (ω = 1600 rpm, v = 10 mV s^{-1}). Scans started at 0.05 V): (a,b) disk current densities. (c,d) ring current densities (curves normalized by N - the collection efficiency (0.26)). (e,f) Selectivity for hydrogen peroxide production ($S_{H_2O_2}$) and (g,h) number of electrons transferred (n) during ORR at varying potentials. The light grey line in the figures indicates the standard potential $E^0_{O2/H2O2}$ = 0.695 V *vs*. RHE.

The LSV curves for the bare GNR (Figs. 5a and 5c) show that the onset potential of the ORR (observed through the disk curve) coincides with the onset potential of H_2O_2 formation (observed through the ring curve), and both appear at high overpotentials — ca. 0.3 V *vs.* RHE, while the thermodynamically expected standard electrode potential for the O_2/H_2O_2 is 0.695 V *vs.* RHE — this points to a low ORR activity for the metal-free carbon catalyst. Although GNR shows low activity for ORR, the values related to S_{H2O2} and *n* (Figs. 5e and 5g) reveal that the ORR occurs with high selectivity for H_2O_2 production through a $2e^-$-transfer pathway, and the production of H_2O_2 reaches up to over 90% ($n = 2.2$) at <0.2 V *vs.* RHE; this is perfectly in line with the findings of previous studies reported in the literature [42,65]. In general, when the GNR matrix is blended with metallic nanoparticles in the presence of low contents of Au-Pd or Pd decorated or not with MoO_x, a synergic effect is observed in the ORR activity. Compared to the unmodified GNR, the modified GNR/Metal catalysts (c.f. Figs. 5e-h) exhibited an increase in catalytic activity of ca. 460 mV (on average) at the onset potential of ORR while the selectivity of these modified catalysts toward H_2O_2 generation was relatively high, at 75% ($n = 2.6$) on average, in the potential range of 0.05 - 0.7 V *vs.* RHE. Due to its oxygenated and nitrogenated groups that help in the anchorage of metallic particles, GNR has been shown to be the most effective supporting material when it comes to the dispersion of metal nanoparticles; apart from that, GNR is found to exhibit a greater metal-support interaction and a higher selectivity for H_2O_2 generation in comparison with carbon black materials (i.e., Vulcan)[42]. Figure S16 presents a comparative analysis, in terms of ORR activity and selectivity, for $AuPdMoO_x$ supported on Vulcan XC-72 and on GNR. Although the GNR/$AuPdMoO_x$ and Vulcan/$AuPdMoO_x$ catalysts had very similar metal loadings (ca. 6 wt.%, c.f. Table S3), the results obtained from the RRDE analysis revealed that the use of Vulcan (which exhibits relatively lower contents of N- and O-functional groups compared to GNR[42]) resulted in lower diffusion-limited current density (ca. 2.9 mA cm^{-2}) for the disk electrode as well as lower selectivity for H_2O_2 generation (ca. 47%) in comparison with the GNR (which presented ca. 3.5 mA cm^{-2} of diffusion-limited current density and ca. 71% of selectivity), evidencing the role of the carbon support in ORR activity. These results are totally in line with those previously reported for the Pd monometallic catalyst systems[42]. Although one notices the presence of low 2e- reduction currents (observed via the oxidation current from the ring) starting at a potential higher than the theoretical potential (0.695 V *vs.* RHE) for the GNR/AuPd, GNR/AuPdMoO_x, Vulcan/AuPdMoO_x, and GNR/PdMoO_x catalysts, based on the Nernst equation, a higher onset potential for H_2O_2 production should be expected at the beginning in the absence of H_2O_2[66].

A comparative analysis of the ORR activity and selectivity between GNR/AuPd and GNR/AuPdMoO_x (Figs. 5a, c, e, g) using the LSV curves shows that the presence of low MoO_x content (0.4 wt.%) resulted in a slight increase in the ORR onset potential (~50 mV) while the selectivity toward H_2O_2 production was practically the same (~71%; $n = 2.7$) in the potential range between 0.05 and 0.7 V *vs.* RHE. As can be noted from the LSV curves, the modification of GNR with a low content of Pd only (Figs. 5b,d,f,h) causes a displacement of 110 mV for the ORR onset potential while the modification of GNR/Pd with MoO_X leads to a slight increase in selectivity toward H_2O_2 production from 73% to 77 %.

As aforementioned, previous studies have suggested that, for Au/Pd-based catalysts, the active sites of Pd are responsible for the improvement in oxygen adsorption, while Au sites contribute toward inhibiting the cleavage of the O-O bond. In this sense, the combined application of these two metals may lead to an increase in ORR activity and higher selectivity toward H_2O_2 production compared to the pure application of these metals individually [67–69]. These observations are in good agreement with the results obtained for the GNR/AuPd, GNR/AuPdMoO$_x$, GNR/Au, and GNR/AuMoO$_x$ catalysts (c.f. Figs. 5 and S14).

When applied in O_2-saturated 0.1 M $HClO_4$, the GNR/Au catalyst presents much worse current densities and negative overpotential, in terms of $E^0_{O2/H2O2}$ = 0.695 V *vs.* RHE, compared to the GNR/Pd catalyst (c.f. Fig. S14 and 5); as such, the former (GNR/Au) is less effective for H_2O_2 production. Similarly, the GNR/Pd catalyst presents a slightly worse current densities and negative overpotential, in terms of $E^0_{O2/H2O2}$ = 0.695 V *vs.* RHE, in comparison with GNR/AuPd, GNR/AuPdMoO$_x$, and GNR/PdMoO$_x$ (c.f. Fig. 5); this evidently points to the importance of the combined application of Au, Pd, and MoO$_x$ in the production of highly efficient electrocatalyst for H_2O_2 production, mostly in acidic medium.

It is worth mentioning that, in the case of the GNR/AuPd, GNR/AuPdMoO$_x$, GNR/Pd and GNR/PdMoO$_x$ catalysts, it appears that the exposure of a surface constituted by a mix of different crystalline structures converges toward high catalytic activity and selectivity for H_2O_2 formation. However, the HR-TEM, SAED and XRD results obtained showed that the dominant crystallographic structures present on the surfaces of the catalysts were (111) and (200) planes which corresponded to *fcc* structures of Pd and Au; these crystalline planes are considered highly active and stable [27,70]. In the case of Au and AuPd (containing diluted Pd concentration), the surfaces with the dominant (111) plane are found to favor the occurrence of ORR via a 2e$^-$-transfer pathway in acidic media [17,27,70,71]; this is quite in line with the results obtained in this study and can possibly be associated with the high selectivity exhibited by the GNR/AuPd, GNR/AuPdMoO$_x$ and GNR/Au catalysts. It is particularly clear that for Pd-based catalysts, the dominant (111) planes are known to favor the occurrence of ORR through a 4e$^-$ transfer pathway in acidic media; however, other factors such as low loading, large inter-particle distances, and strongly adsorbing species (i.e., halides, surfactants, and bi(sulfate) anion) also play an important complementary role and help favor H_2O_2 formation[72].

In general, the role of different active metal sites like Au, Pd, and Mo in ORR, in terms of the formation of H_2O_2 instead of H_2O, from the point of view of intermediate adsorption, can be found clearly explained in a recent work authored by Zhao and Liu [73]. As demonstrated in reference 73, the initial adsorption of O_2 in the Pd atom surrounded by Au atoms (GNR/AuPd catalyst) promotes the occurrence of the first charge transfer and proton addition, which leads to *−O−OH (* = active site) adsorption in the Pd atom (c.f. Figure 6a). The second electron transfer and proton addition preferentially involve the bond cleavage of *−O, instead of the bond breakage of O−OH, and leads to the release of H_2O_2. Zhao and Liu [73] showed that the activation energy of *−O bond breakage is lower than that of O−OH bond breakage for Pd/Au alloy (kinetic origin of selectivity toward H_2O_2 production) even when the final state of O−OH bond breakage presents lower energy (thermodynamically more favorable [26,73]) than that of *−O bond breakage. Also, the authors [73] found out that in acid conditions and under diminishing potentials, the difference in energy barrier will decrease for both *−O and O−OH bond breakages; furthermore, the reduction in energy barrier will be more accentuated for *−O bond, and this leads to the enhancement of selectivity for H_2O_2 formation. These observations help explain the experimental results obtained in our present study (Fig. 5 and later in Fig. 7). While the phenomenon involving the absorption of reaction intermediates observed on the surface of GNR/AuPdMoO$_x$ - with the presence of MoO$_x$, is likely to be similar to that observed on the surface of GNR/AuPd, the O−OH bond is found to be even further away from the GNR/AuPd surface due to the steric effect of oxygen present in the MoO$_x$ cluster relative to the O from the O−OH group (c.f. Figure 6b), and this tends to increase the selectivity for H_2O_2 formation as observed in the present work (Figures 5 and 7).

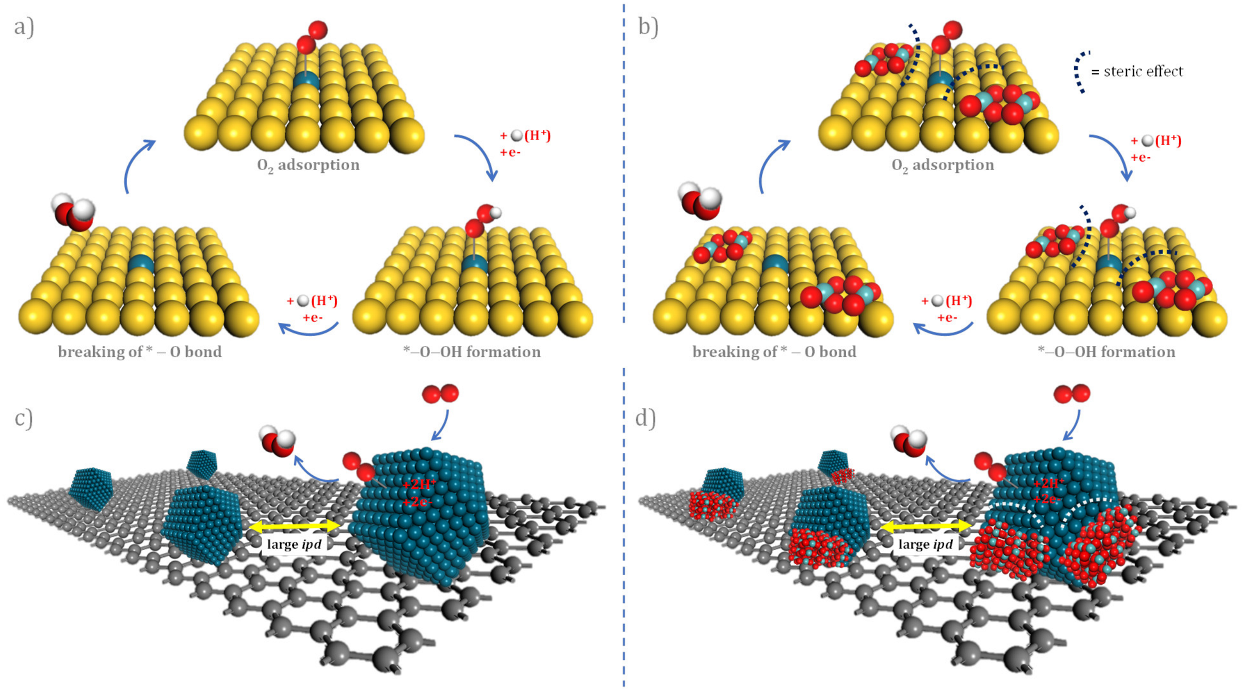

Figure 6. Schematic representation of the pathways involving H_2O_2 generation on the (a) GNR/AuPd, (b) GNR/AuPdMoO$_x$, (c) GNR/Pd, and (d) GNR/PdMoO$_x$ catalysts surfaces. The atoms are represented as follows: Au-gold; Pd-dark cyan; Mo-cyan; C-gray; O-red; H-white.

With regard to Pd-based monometallic catalysts, reports in the literature have shown that the use of low Pd loadings (<2 wt. %) and large interparticle distance tends to suppress the re-adsorption of H_2O_2 generated in the first stage of ORR. In this sense, the suppression of H_2O_2 re-adsorption hinders the further reduction of H_2O_2 for the production of water [33,42,74], and this leads to high selectivity toward H_2O_2 production; this phenomenon helps explain the electrocatalytic performance of GNR/Pd and GNR/PdMoO$_x$ catalysts in ORR (c.f. Figure 6c,d). It is worth noting that although the application of AuPd-based catalysts (GNR/AuPd and GNR/AuPdMoO$_x$) resulted in relatively higher onset potentials for ORR compared to Pd-based catalysts (GNR/Pd and GNR/PdMoO$_x$), the results obtained from the RRDE analysis suggest that the geometric effect caused by the Au-Pd alloy was less significant under low metal loading conditions; in other words, with Pd loading maintained at ≤ 2.0 wt.%, ORR can occur in conditions of high catalytic activity and selectivity for H_2O_2 - which can be as high as or even higher than the classic Au-Pd systems - due to the suppression of H_2O_2 re-adsorption effect. It is worth noting that although the nanoparticles have displayed a wider variation in size (and shape) and a study on the detailed correlation between particle size and selectivity is outside the scope of this work, studies reported in the literature have documented the conclusive effect of particle size only for the full reduction of O_2 to H_2O [75]. In general, such big differences in selectivity observed for different loading/ipd are not observed when the particle size is changed [42,76].

With regard to the influence of MoOx, it is expected that the presence of oxophilic species on the surface of the catalyst acts as a driving force capable of fueling the movement of AuPd to the interior region of the nanoparticles with a view to decreasing the surface energy and reducing the amount of active sites on the surface of the catalyst. Xu et al.[30] employed a combination of Sabatier analysis and DFT to show that Pd-based alloy catalysts can present enhanced activity and selectivity toward the thermocatalytic synthesis of H_2O_2 depending on the electronegativity of the dopants that withdraw electrons from Pd atoms. The authors suggested that in the case of PdAu-based ternary alloy catalysts doped with metal presenting electronegativity close to Pd — as is the case of Mo, the metal(Mo) may form oxides after calcination; the formation of these oxides may result in the encapsulation of small Pd-rich particles, and this can prevent the decomposition and hydrogenation of H_2O_2 (responsible for H_2O formation as the main product), which may in turn contribute to the improvement of catalytic activity and selectivity toward the thermocatalytic production of H_2O_2 for the Au-Pd-Mo nanocatalyst - for example. Furthermore, in the electrocatalytic synthesis of H_2O_2, the reduction of the amount of active Pd sites on the catalyst surface can influence the adsorption of O_2 on these sites, leading to changes in the selectivity and possibly the long-term stability of ORR [65].

3.3. Stability test of the electrocatalysts

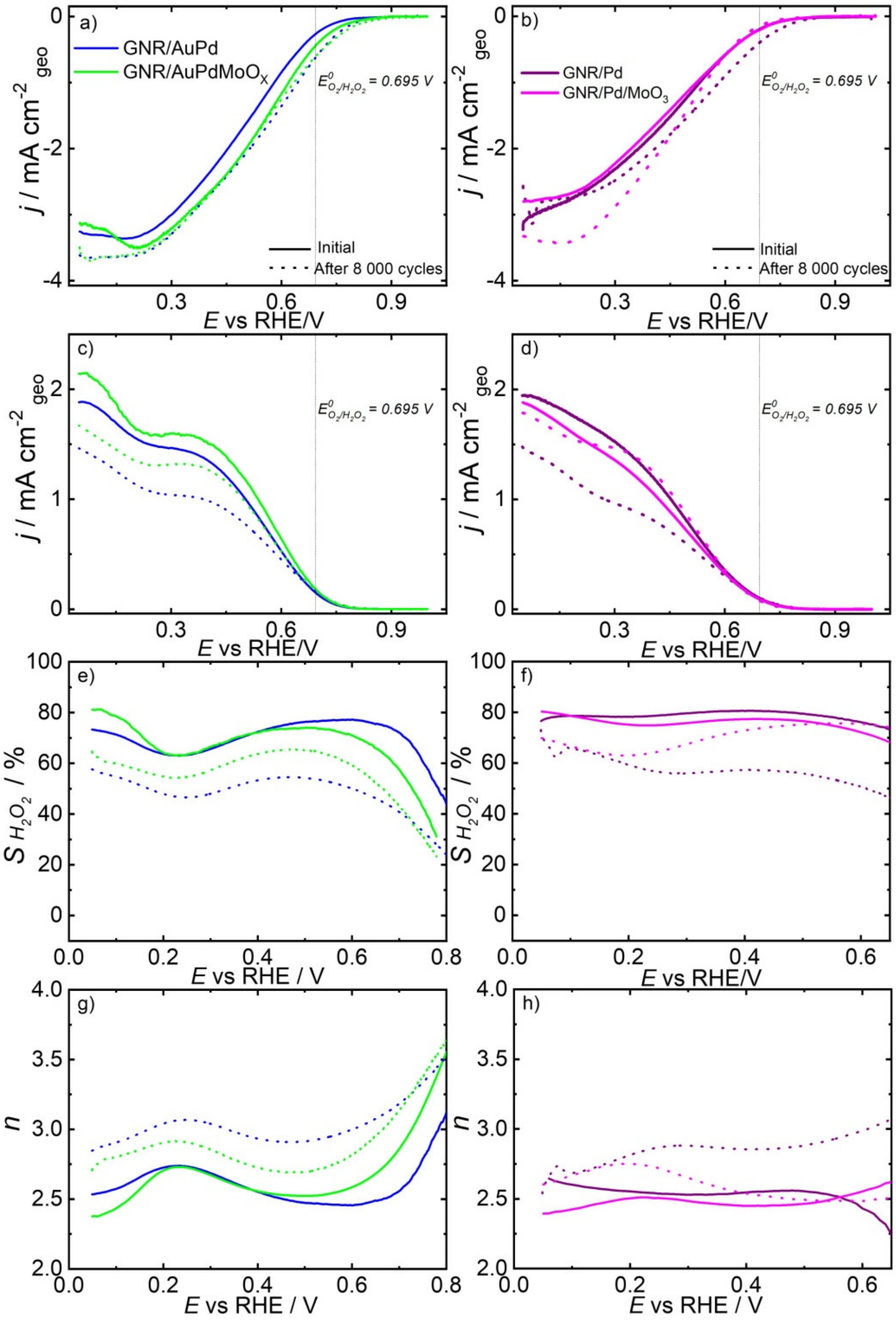

Figure 7. Results obtained from the linear sweep analysis conducted using RRDE for GC modified with GNR/Metals catalysts employed in O_2-saturated 0.1 M $HClO_4$ (ω = 1600 rpm, v = 10 mV s^{-}

^{1}) before and after the stability test: (a,b) disk current densities; (c,d) ring current densities (curves normalized by N - the collection efficiency (0.26)); (e,f) selectivity for peroxide production ($S_{H_2O_2}$); and (g,h) the number of electrons transferred (n) during the ORR at varying potentials.

Figure 7 presents a comparative analysis of the LSV curves for the non–electrochemically (before) and electrochemically stabilized (after AST) GNR/AuPd, GNR/AuPdMoO$_x$, GNR/Pd, and GNR/PdMoO$_x$ catalysts. The comparison of the LSV curves showed that the disk and ring current densities of the GNR/AuPdMoO$_x$and GNR/PdMoO$_x$ samples suffered the smallest variations after the AST. On the other hand, the LSV curves related to the disk electrode obtained after the AST for the GNR/AuPd and GNR/Pd catalysts exhibited a marked shift toward more positive potentials compared to the LSV curves obtained prior to the stability test. In addition, the ring electrode exhibited a decrease in current density after AST. These significant changes in the LSV curves for the GNR/AuPd and GNR/Pd catalysts suggest that, after AST, the catalyst surface becomes slightly more active for ORR and less selective for H_2O_2 production. The changes can be attributed to the residual surfactant (c.f. Figure S16) and the chloride ions that were left after the synthesis procedure; these residual substances were removed during the potential cycling (AST), and this resulted in a greater exposure of the Pd surface (c.f. CV profiles for GNR/AuPdMoO$_x$ after AST in Fig. S17). As pointed out in the literature, surfactants, ionomers, and halides are expected to have surface blocking effects on Pd and Pt, and these effects typically favor H_2O_2 production [31,33,34,77].

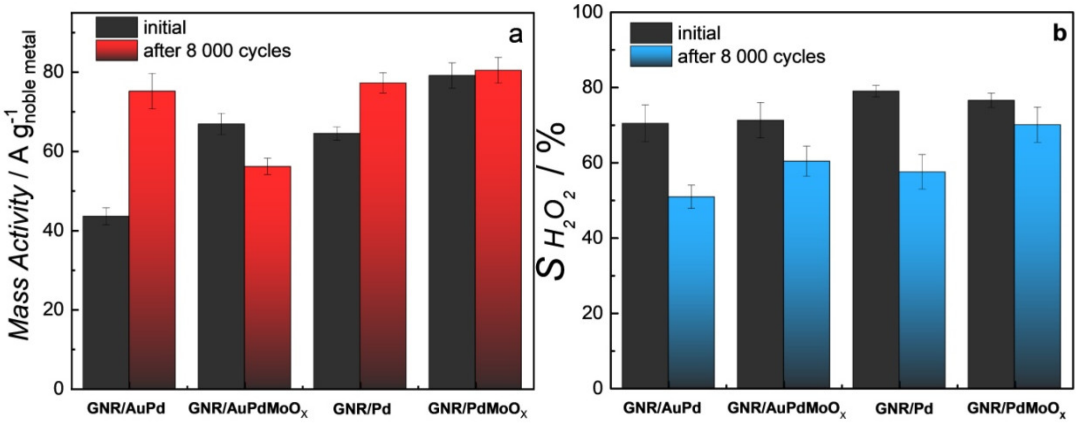

Figure 8. (a) Values related to mass activity obtained at an overpotential of 50 mV for different GNR/metal-based catalysts applied in O_2-sat 0.1 M $HClO_4$ before and after the stability test (values were estimated from the ring curves of the RRDE results shown in Figure 6). (b) Average selectivity (%) for H_2O_2 production in the potential range of 0.05 - 0.6 V *vs.* RHE.

In Figure 8, one can see the values related to mass activity (*MA*) obtained from the curves of the ring electrode at an overpotential of 50 mV (0.645 V *vs.* RHE), as described elsewhere[42], along with the selectivity for H_2O_2 generation ($S_{H_2O_2}$); this figure provides one with a clearer picture of the impact caused by the AST on ORR activity and selectivity for the catalysts investigated here. For GNR/AuPd and GNR/Pd, the *MA* for the production of H_2O_2 increased from 53.9 to 76.2 A $g^{-1}_{noble\ metal}$ (on average), while the selectivity toward H_2O_2 generation ($S_{H_2O_2}$) decreased from 75 to 54% (on average) after AST. For GNR/AuPdMoO$_x$ and GNR/PdMoO$_x$, the *MA* for the production of H_2O_2 slightly changed from 72.9 to 68.3 A $g^{-1}_{noble\ metal}$, while the $S_{H_2O_2}$ changed from 74 to 65% after the AST. The higher stabilization observed in the values of *MA* and $S_{H_2O_2}$ for the GNR/AuPdMoO$_x$ and GNR/PdMoO$_x$ catalysts in comparison with the GNR/AuPd and GNR/Pd catalysts can be attributed to the presence of low amount of MoOx (~0.4 wt.%), which led to a smaller variation in the catalytic activity for ORR and a smaller deviation of the selectivity for H_2O_2 production after the AST; these results show that the presence of MoOx on the surface of Au-Pd and Pd nanoparticles contribute to an increase in the electrochemical stability of the catalysts - this does not depend on the permanence of the surfactant residues and chloride ions to ensure high selectivity for H_2O_2 production. The improvement in electrochemical stability is linked to the passivation caused by the presence of MoOx on the catalyst surface which generates a driving force capable of pushing the Au/Pd to the interior region of the catalyst and promoting a decrease in the surface energy of the catalyst; the decrease in surface energy causes a reduction in the amount of active centers present on the catalyst surface [78,79]. This observation is in line with the results obtained from XPS analysis (c.f. Figure 3, Table S5) which showed less amount of Pd in oxidized state (lower % content of PdO in comparison with Pd^0) in the presence of MoOx. Previous studies reported in the literature have also pointed out a decrease in the surface energy of noble metals observed for catalysts constructed using highly oxophilic metals such as Ti[65,78,79].

With regard to the stability of Mo, the oxide species (MoO_2 and MoO_3) tend to be more stable in acidic conditions than in alkaline conditions [80,81]; however, in a narrow range at low potential (ca. 0 to 0.1 V) and low pH, MoOx may be dissolved as Mo^{3+} or be further reduced as metallic Mo at lower potentials (ca. < 0 V)[80,81]. To evaluate whether MoOx could be reduced during the experimental conditions of ORR, the XRD patterns were measured for the GNR/AuPdMoO_X catalyst before and after the stability test; the results obtained are shown in Fig. S18. As can be noted, there were no significant differences between the XRD patterns recorded before and after the stability test; this shows that the MoOx species remained stable even after the stability test. In addition, the HR-TEM images recorded after the stability test (Fig. S4) also pointed to the electrochemical stability of MoOx species, once there were no lattice fringes that are typically characteristic of metallic Mo structure.

3.4. Influence of supporting electrolyte

The ORR activity and selectivity of the GNR/AuPdMoO$_x$ and GNR/PdMoO$_x$ catalysts were additionally investigated using O$_2$-saturated 0.5 M H_2SO_4 and 0.1 M KOH solutions; the results obtained were compared with those obtained using 0.1 M $HClO_4$ (see Figure 9).

The GNR/AuPdMoO$_x$ catalyst recorded dramatic changes in the ORR onset potential and in the diffusion-limited current density when the electrolyte was modified. When the 0.5 M H_2SO_4 electrolyte solution was applied, the LSV curves (Fig. 9) showed that ORR occurred at approximately 0.77 V *vs*. RHE, while the reaction occurred at around 0.82 *vs*. RHE when 0.1 M $HClO_4$ solution was employed. The disk current densities were also drastically affected; the current densities obtained ranged from 3.5 to 2.4 mA cm^{-2}; these values led to an increase in selectivity for H_2O_2 production from approximately 71% (in 0.1 M $HClO_4$) to 82% (in 0.1 M H_2SO_4) (c.f. Figure S19). When 0.1 M KOH solution was applied, the ORR onset potential changed to about 1.0 V *vs.* RHE and the diffusion-limited current density recorded values around 4.3 mA cm^{-2}; furthermore, a dramatic decrease was also observed in the maximum current densities of the ring electrode (from 2.1 to 1.2 mA cm^{-2}). Based on the changes observed in the LSV curves, the selectivity for H_2O_2 (HO_2^- in alkaline medium) production decreased drastically to approximately 41% (c.f. Figure S19); this outcome implies that ORR in the GNR/AuPdMoO$_x$ catalyst in alkaline medium occurs most favorably via the 4e$^-$ pathway (*n*= 3.2 on average), and the mechanism leads to the formation of OH$^-$ as the main product.

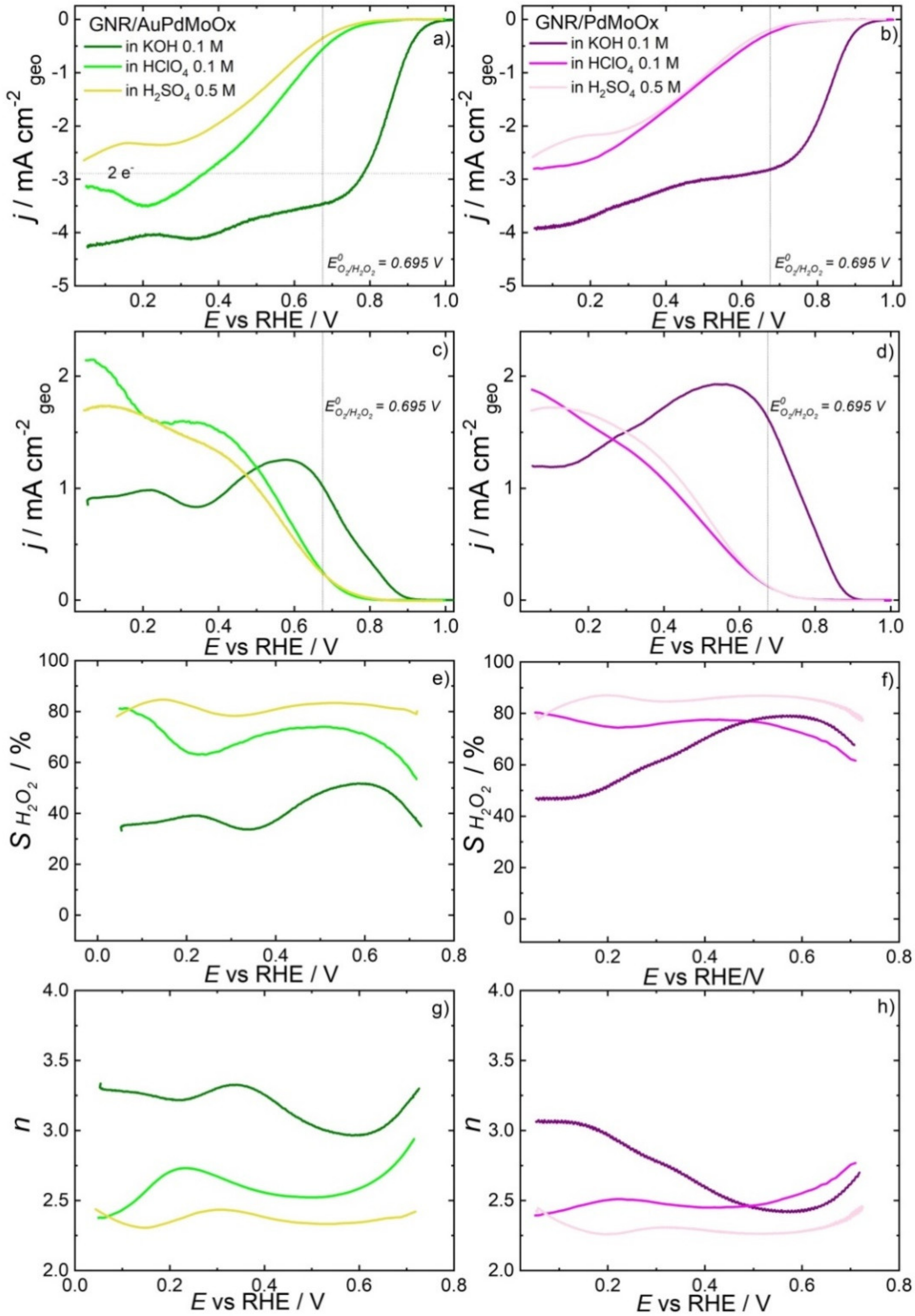

Figure 9. Results obtained from the linear sweep analysis conducted using RRDE for GC modified with GNR/AuPdMoO$_x$ or GNR/PdMoO$_x$ employed in O$_2$-saturated solutions of 0.1 M HClO$_4$, 0.1 M KOH and 0.5 M H$_2$SO$_4$(ω = 1600 rpm, v = 10 mV s^{-1}): (a,b) disk current densities. (c,d) ring current densities (curves normalized by N - the collection efficiency (0.26)). (e,f) Selectivity for peroxide production ($S_{H_2O_2}$) and (g,h) number of electrons transferred (n) during ORR at varying potentials.

In the case of the GNR/PdMoO$_x$ catalyst, slight variations were observed in the ORR activity and selectivity when the supporting electrolyte was changed from $HClO_4$ to H_2SO_4. The LSV curves showed that the ORR onset occurred at ca. 0.77 V *vs*. RHE for both solutions and that the disk current densities recorded a slight decrease (on average) from 2.7 to 2.3 mA cm^{-2} at potential lower than 0.4 V *vs*. RHE. These changes in the LSV curves led to an increase in selectivity for H_2O_2 production from ca. 77% (in $HClO_4$ 0.1 M) to ca. 85% (in H_2SO_4 0.1 M, c.f. Figure S19). In alkaline medium, the ORR onset potential changed to ca. 0.92 V *vs*. RHE, and the LSV curves for the disk and ring electrodes exhibited two plateaus with diffusion-limited current densities in the potential ranges of 0.70−0.4 and 0.4 to 0.05 V *vs*. RHE; the disk electrode recorded current densities of 3.0 and 3.9 mA cm^{-2} and the ring electrode recorded densities of 1.9 and 1.2 mA cm^{-2}. In view of that, the selectivity for H_2O_2 production in the first two levels of current density was ca. 76% and 55%, respectively. These values reflect an average selectivity of 63% within both potential ranges (c.f. Figure S19); in essence, the values show that ORR takes place under a condition of high selectivity for H_2O_2 production (>60%) on the surface of the GNR/PdMoO$_x$ catalyst in the three media investigated. Table S6 presents a comparative analysis of ORR parameters for state-of-the-art catalysts used for H_2O_2 electroproduction obtained via the application of a RRDE setup. It can be observed that, in general, the GNR/AuPdMoO$_x$ and GNR/PdMoO$_x$ catalysts exhibited superiority in several ORR parameters, including onset potential (E_{onset}), half-wave potential ($E_{1/2}$), and cathode current density (*j* at 0.2 V *vs*. RHE) in comparison with other state-of-the-art catalysts. One of the major highlights in Table S6 is related to the superior performance of the GNR/PdMoO$_x$ catalyst over other Pd and Pt-based catalysts in terms of H_2O_2 electroproduction in acid medium; the GNR/PdMoO$_x$ catalyst presented (to the best of the authors' knowledge) the highest E_{onset} (0.92 V *vs*. RHE), $E_{1/2}$ (0.82 V *vs*. RHE), and *MA* (6.6 mA $g^{-1}_{noble\ metal}$) values with selectivity of 63% in a wide potential range (from 0.1 to 0.8 V *vs*. RHE) in alkaline medium.

Both the GNR/AuPdMoO$_x$ and GNR/PdMoO$_x$ catalysts displayed similar patterns of behavior when H_2SO_4 was employed as electrolyte. The two catalysts presented a lower ORR activity combined with a higher selectivity for H_2O_2 production; these results are in good agreement with the results reported in previous studies related to the application of Pd, Pt, and Au-based catalysts in perchloric and sulfuric acid media [5,82–84]. This observed decrease in ORR activity can be attributed to the blocking effect caused by the (bi-)sulfate anions which undergo adsorption on the surface of Pd and Au, lowering the availability of active sites and slightly favoring the generation of H_2O_2[5,82–85]. By contrast, in alkaline medium, the GNR/AuPdMoO$_x$ catalyst presented drastic changes in ORR activity and selectivity for ORR in comparison with the GNR/PdMoO$_x$catalyst; this can be attributed to the structural effects of Au in alkaline solution. Studies related to the application of Au nanocrystals, especially involving the use of Au (100) surface, reported improvements in ORR activity as well as in selectivity toward OH^- production in alkaline medium; these studies also showed that, in acidic medium, ORR typically operates at higher overpotentials with greater selectivity for H_2O_2 production [18,19,23]. In line with the findings of previous studies reported in the literature and the results obtained for the GNR/AuPdMoO$_x$ catalyst, LSV curves constructed for the bulk polycrystalline Au electrode (Fig. S20) showed an increase in ORR activity concomitantly with a decrease in selectivity for H_2O_2 production when the medium was changed from $HClO_4$ to KOH. Also, in contrast to Au-based catalysts, previous studies reported in the literature related to shape-controlled Pd nanoparticles have shown that there is no structure dependence for ORR activity and selectivity in alkaline electrolytes [72,86]. These observations are also in good agreement with the results obtained for GNR/PdMoOx in this present study.

4. Conclusions

In summary, the present study demonstrated the successful synthesis and characterization of the proposed electrocatalysts constructed using low contents (≤6.4 wt.%) of Au, Pd and Mo combined with GNRs. The synthesized GNR/Pd, GNR/AuPd, GNR/PdMoO$_x$, and GNR/AuPdMoO$_x$ catalysts presented improvements in ORR activity and selectivity for hydrogen peroxide production in acidic medium; the good results obtained were attributed to the following set of factors: geometric and steric effects, low Pd loadings, large interparticle distance, as well as site blocking effect caused by the surfactant residues and anions (bi-sulfate) from the supporting electrolyte. The RRDE results showed that the geometric effect caused by the Au-Pd alloy was less significant under conditions in which low contents of metals were employed; in other words, conditions in which Pd loading was kept at ≤2 wt.%. The findings showed that ORR occurred in conditions of high catalytic activity with a high degree of selectivity toward H_2O_2 production due to the suppression of the re-adsorption of H_2O_2.

The application of the catalysts containing Mo (GNR/PdMoO$_x$ and GNR/AuPdMoO$_x$) led to the enhancement of electrochemical stability toward H_2O_2 production, which was attributed to the presence of MoO$_x$ in the catalysts (specifically associated with the oxyphilic character of MoO$_x$). The MoO$_x$ acted as a driving force that pushed the Au/Pd to the interior side of the catalyst, leading to a decrease in the surface energy and a reduction in the number of active centers on the catalyst surface; these events helped maintain the selectivity of the catalyst for H_2O_2 production.

The GNR/PdMoO$_x$ catalysts containing low Pd contents (1.9 wt.%) presented similar ORR catalytic behavior in both 0.1 $HClO_4$ and 0.5 M H_2SO_4 solutions, as well as higher selectivity for H_2O_2 production in 0.1 KOH compared to the GNR/AuPdMoO$_x$ catalyst. Furthermore, in comparison with other state-of-the-art catalysts, the GNR/PdMoO$_x$ catalyst exhibited (to the best of the authors' knowledge) the highest E_{onset}(0.92 V *vs*. RHE), $E_{1/2}$ (0.82 V *vs*. RHE), and *MA* (6.6 mA $g^{-1}_{noble\ metal}$) values, with selectivity of 63% in a wide potential range (from 0.1 to 0.8 V *vs*. RHE) in alkaline medium; these factors clearly point to the catalytic efficiency and versatility of the GNR/PdMoO$_x$ catalyst. The findings of the present study shed light on the efficiency of the proposed electrocatalysts and provide useful insights into the development and implementation of new, selective and stable catalytic materials which are economically viable and actively efficient for the electrocatalytic production of H_2O_2.

ASSOCIATED CONTENT

Supporting Information. The supporting information contains additional experimental details, materials, methods, including tables and figures related to supplementary results and references. This material is available free of charge via the internet at:

ORCID

Guilherme V. Fortunato: 0000-0002-0768-4156
Leticia Siqueira Bezerra: 0000-0003-2077-2123
Matheus S. Kronka: 0000-0002-8518-2960
Eduardo S. F. Cardoso:0000-0003-4532-1089
Alexsandro J. Santos: 0000-0002-5408-2238
Jorge L. R. Júnior: 0000-0001-9716-8472
Marcos R.V. Lanza: 0000-0002-8285-7838
Gilberto Maia: 0000–0003–2449–0887

Author Contributions

The manuscript was written through contributions from all the authors. All the authors have given their approval of the final version of the manuscript.

Notes

The authors declare no competing financial interest.

ACKNOWLEDGMENTS

The authors are grateful to the LNNano/CNPEM and the LCE/DEMa/UFSCar for their support in the conduct of TEM analyses, the LAMAS – Laboratório Multiusuário de Análise de Superfícies, from UFRGS for providing the XPS facilities, and the Department of Interface Chemistry and Surface Engineering - Max-Planck-Institut für Eisenforschung GmbH for helping with the XRD facilities. The authors acknowledge the financial support provided by the following Brazilian research funding agencies: the National Council for Scientific and Technological Development - CNPq (grants # 303759/2014-3, 303351/2018-7, and 405742/2018-5, #465571/2014-0, #302874/2017-8 and #427452/2018-0), São Paulo Research Foundation (FAPESP – grants #2014/50945-4, #2017/23464-3, #2017/10118-0, and #2019/04421-7, #2019/20634-0), Fundect-MS (grant # 59/300.184/2016), CAPES-PRINT (grant 88881.311799/2018-01), and the Coordenação de Aperfeiçoamento de Pessoal de Nível Superior (CAPES – Finance Code 001). L.S.B. and E.S.F.C are grateful to CAPES for the individual fellowship granted in support of their research.

REFERENCES AND NOTES

(1) Myers, R. L. *The 100 Most Important Chemical Compounds: A Reference Guide*, 1st ed.; Greenwood Press: Westport, CT, 2007; p 352.

(2) Pulidindi, K.; Pandey, H. Hydrogen peroxide market size worth over $6.2 billion by 2026 https://www.gminsights.com/pressrelease/hydrogen-peroxide-market (accessed 2021 -01 - 12).

(3) Pulidindi, K.; Pandey, H. *Hydrogen Peroxide Market Size by End-User Industry (Paper & Pulp, Chemical, Waste Water Treatment, Mining), Industry Analysis Report, Regional Outlook, Application Potential, Price Trends, Competitive Market Share & Forecast, 2020 – 2026*; GMI851; Delaware, 2020.

(4) Campos-Martin, J. M.; Blanco-Brieva, G.; Fierro, J. L. G. Hydrogen Peroxide Synthesis: An Outlook beyond the Anthraquinone Process. *Angew. Chemie - Int. Ed.* **2006**, *45* (42), 6962–6984.

(5) Perry, S. C.; Pangotra, D.; Vieira, L.; Csepei, L.-I.; Sieber, V.; Wang, L.; Ponce de León, C.; Walsh, F. C. Electrochemical Synthesis of Hydrogen Peroxide from Water and Oxygen. *Nat. Rev. Chem.* **2019**, *3* (7), 442–458.

(6) Siahrostami, S.; Verdaguer-Casadevall, A.; Karamad, M.; Deiana, D.; Malacrida, P.; Wickman, B.; Escudero-Escribano, M.; Paoli, E. A.; Frydendal, R.; Hansen, T. W.; Chorkendorff, I.; Stephens, I. E. L.; Rossmeisl, J. Enabling Direct H_2O_2 Production through Rational Electrocatalyst Design. *Nat. Mater.* **2013**, *12* (12), 1137–1143.

(7) Verdaguer-casadevall, A.; Deiana, D.; Karamad, M.; Siahrostami, S.; Malacrida, P.; Hansen, T. W.; Rossmeisl, J.; Chorkendorff, I.; Stephens, I. E. L. Trends in the Electrochemical Synthesis of H_2O_2: Enhancing Activity and Selectivity by Electrocatalytic Site Engineering. *Nano Lett.* **2014**, *14* (3), 1603–1608.

(8) Yang, S.; Verdaguer-Casadevall, A.; Arnarson, L.; Silvioli, L.; Čolić, V.; Frydendal, R.; Rossmeisl, J.; Chorkendorff, I.; Stephens, I. E. L. Toward the Decentralized Electrochemical Production of H_2O_2: A Focus on the Catalysis. *ACS Catal.* **2018**, *8* (5), 4064–4081.

(9) Brillas, E.; Alcaide, F.; Cabot, P. L. A Small-Scale Flow Alkaline Fuel Cell for on-Site Production of Hydrogen Peroxide. *Electrochim. Acta* **2002**, *48* (4), 331–340.

(10) Jung, E.; Shin, H.; Hooch Antink, W.; Sung, Y.-E.; Hyeon, T. Recent Advances in Electrochemical Oxygen Reduction to H_2O_2: Catalyst and Cell Design. *ACS Energy Lett.* **2020**, *5* (6), 1881–1892.

(11) Siahrostami, S.; Villegas, S. J.; Bagherzadeh Mostaghimi, A. H.; Back, S.; Farimani, A. B.; Wang, H.; Persson, K. A.; Montoya, J. A Review on Challenges and Successes in Atomic-Scale Design of Catalysts for Electrochemical Synthesis of Hydrogen Peroxide. *ACS Catal.* **2020**, *10* (14), 7495–7511.

(12) Kocha, S. S. Electrochemical Degradation: Electrocatalyst and Support Durability. In *Polymer Electrolyte Fuel Cell Degradation*; Mench, M., Kumbur, E. C., Veziroglu, T. N., Eds.; Academic Press: Oxford, 2012; pp 89–214.

(13) Pizzutilo, E.; Freakley, S. J.; Cherevko, S.; Venkatesan, S.; Hutchings, G. J.; Liebscher, C. H.; Dehm, G.; Mayrhofer, K. J. J. Gold-Palladium Bimetallic Catalyst Stability: Consequences for Hydrogen Peroxide Selectivity. *ACS Catal.* **2017**, *7* (9), 5699–5705.

(14) Pizzutilo, E.; Freakley, S. J.; Geiger, S.; Baldizzone, C.; Mingers, A.; Hutchings, G. J.; Mayrhofer, K. J. J.; Cherevko, S. Addressing Stability Challenges of Using Bimetallic Electrocatalysts: The Case of Gold–Palladium Nanoalloys. *Catal. Sci. Technol.* **2017**, *7* (9), 1848–1856.

(15) Jirkovský, J. S.; Halasa, M.; Schiffrin, D. J. Kinetics of Electrocatalytic Reduction of Oxygen and Hydrogen Peroxide on Dispersed Gold Nanoparticles. *Phys. Chem. Chem. Phys.* **2010**, *12* (28), 8042.

(16) Pizzutilo, E.; Kasian, O.; Choi, C. H.; Cherevko, S.; Hutchings, G. J.; Mayrhofer, K. J. J.; Freakley, S. J. Electrocatalytic Synthesis of Hydrogen Peroxide on Au-Pd Nanoparticles: From Fundamentals to Continuous Production. *Chem. Phys. Lett.* **2017**, *683*, 436–442.

(17) Viswanathan, V.; Hansen, H. A.; Rossmeisl, J.; Nørskov, J. K. Unifying the 2e – and 4e – Reduction of Oxygen on Metal Surfaces. *J. Phys. Chem. Lett.* **2012**, *3* (20), 2948–2951.

(18) Jusys, Z.; Behm, R. J. The Effect of Anions and PH on the Activity and Selectivity of an Annealed Polycrystalline Au Film Electrode in the Oxygen Reduction Reaction-Revisited. *ChemPhysChem* **2019**, *20* (24), 3276–3288.

(19) Adić, R. R.; Marković, N. M.; Vešović, V. B. Structural Effects in Electrocatalysis. *J. Electroanal. Chem. Interfacial Electrochem.* **1984**, *165* (1–2), 105–120.

(20) Blizanac, B. B.; Ross, P. N.; Markovic, N. M. Oxygen Electroreduction on Ag(111): The pH Effect. *Electrochim. Acta* **2007**, *52* (6), 2264–2271.

(21) Kulkarni, A.; Siahrostami, S.; Patel, A.; Nørskov, J. K. Understanding Catalytic Activity Trends in the Oxygen Reduction Reaction. *Chem. Rev.* **2018**, *118* (5), 2302–2312.

(22) Zurilla, R. W. The Kinetics of the Oxygen Reduction Reaction on Gold in Alkaline Solution. *J. Electrochem. Soc.* **1978**, *125* (7), 1103.

(23) Prieto, A.; Hernández, J.; Herrero, E.; Feliu, J. M. The Role of Anions in Oxygen Reduction in Neutral and Basic Media on Gold Single-Crystal Electrodes. *J. Solid State Electrochem.* **2003**, *7* (9), 599–606.

(24) Markovic, N. M.; Gasteiger, H. A.; Ross, P. N. Oxygen Reduction on Platinum Low-Index Single-Crystal Surfaces in Sulfuric Acid Solution: Rotating Ring-Pt(hkl) Disk Studies. *J. Phys. Chem.* **1995**, *99* (11), 3411–3415.

(25) Erikson, H.; Liik, M.; Sarapuu, A.; Kozlova, J.; Sammelselg, V.; Tammeveski, K. Oxygen Reduction on Electrodeposited Pd Coatings on Glassy Carbon. *Electrochim. Acta* **2013**, *88*, 513–518.

(26) Jirkovský, J. S.; Panas, I.; Ahlberg, E.; Halasa, M.; Romani, S.; Schiffrin, D. J. Single Atom Hot-Spots at Au–Pd Nanoalloys for Electrocatalytic H_2O_2 Production. *J. Am. Chem. Soc.* **2011**, *133* (48), 19432–19441.

(27) Zhao, X.; Yang, H.; Xu, J.; Cheng, T.; Li, Y. Bimetallic PdAu Nanoframes for Electrochemical H2O2Production in Acids. *ACS Mater. Lett.* **2021**, *3* (7), 996–1002.

(28) Ko, Y.-J.; Choi, K.; Yang, B.; Lee, W. H.; Kim, J.-Y.; Choi, J.-W.; Chae, K. H.; Lee, J. H.; Hwang, Y. J.; Min, B. K.; Oh, H.-S.; Lee, W.-S. A Catalyst Design for Selective Electrochemical Reactions: Direct Production of Hydrogen Peroxide in Advanced Electrochemical Oxidation. *J. Mater. Chem. A* **2020**, *8* (19), 9859–9870.

(29) Montemore, M. M.; van Spronsen, M. A.; Madix, R. J.; Friend, C. M. O_2 Activation by Metal Surfaces: Implications for Bonding and Reactivity on Heterogeneous Catalysts. *Chem. Rev.* **2018**, *118* (5), 2816–2862.

(30) Xu, H.; Cheng, D.; Gao, Y. Design of High-Performance Pd-Based Alloy Nanocatalysts for Direct Synthesis of H_2O_2. *ACS Catal.* **2017**, *7* (3), 2164–2170.

(31) Katsounaros, I.; Meier, J. C.; Mayrhofer, K. J. J. The Impact of Chloride Ions and the Catalyst Loading on the Reduction of H_2O_2 on High-Surface-Area Platinum Catalysts. *Electrochim. Acta* **2013**, *110*, 790–795.

(32) Choi, C. H.; Kwon, H. C.; Yook, S.; Shin, H.; Kim, H.; Choi, M. Hydrogen Peroxide Synthesis via Enhanced Two-Electron Oxygen Reduction Pathway on Carbon-Coated Pt Surface. *J. Phys. Chem. C* **2014**, *118* (51), 30063–30070.

(33) Fortunato, G. V.; Pizzutilo, E.; Cardoso, E. S. F.; Lanza, M. R. V.; Katsounaros, I.; Freakley, S. J.; Mayrhofer, K. J. J.; Maia, G.; Ledendecker, M. The Oxygen Reduction Reaction on Palladium with Low Metal Loadings: The Effects of Chlorides on the Stability and Activity towards Hydrogen Peroxide. *J. Catal.* **2020**, *389*, 400–408.

(34) HeZhong, D.; Gan, S.; Xie, J.; Wang, W.; Liu, Z.; Guo, W.; Yang, X.; Niu, L. Hydrogen Peroxide Electrosynthesis via Regulating the Oxygen Reduction Reaction Pathway on Pt Noble Metal with Ion Poisoning. *Electrochim. Acta* **2021**, 137721.

(35) Wang, N.; Ma, S.; Zuo, P.; Duan, J.; Hou, B. Recent Progress of Electrochemical Production of Hydrogen Peroxide by Two-Electron Oxygen Reduction Reaction. *Adv. Sci.* **2021**, *8* (15), 2100076.

(36) Zhao, H.; Yuan, Z. Y. Design Strategies of Non-Noble Metal-Based Electrocatalysts for Two-Electron Oxygen Reduction to Hydrogen Peroxide. *ChemSusChem* **2021**, *14* (7), 1616–1633.

(37) Zhou, Y.; Chen, G.; Zhang, J. A Review of Advanced Metal-Free Carbon Catalysts for Oxygen Reduction Reactions towards the Selective Generation of Hydrogen Peroxide. *J. Mater. Chem. A* **2020**, *8* (40), 20849–20869.

(38) Sun, Y.; Sinev, I.; Ju, W.; Bergmann, A.; Dresp, S.; Kühl, S.; Spöri, C.; Schmies, H.; Wang, H.; Bernsmeier, D.; Paul, B.; Schmack, R.; Kraehnert, R.; Roldan Cuenya, B.; Strasser, P. Efficient Electrochemical Hydrogen Peroxide Production from Molecular Oxygen on

Nitrogen-Doped Mesoporous Carbon Catalysts. *ACS Catal.* **2018**, *8* (4), 2844–2856.

(39) Sun, Y.; Li, S.; Jovanov, Z. P.; Bernsmeier, D.; Wang, H.; Paul, B.; Wang, X.; Kühl, S.; Strasser, P. Structure, Activity, and Faradaic Efficiency of Nitrogen-Doped Porous Carbon Catalysts for Direct Electrochemical Hydrogen Peroxide Production. *ChemSusChem* **2018**, *11* (19), 3388–3395.

(40) Zhao, K.; Su, Y.; Quan, X.; Liu, Y.; Chen, S.; Yu, H. Enhanced H_2O_2 Production by Selective Electrochemical Reduction of O_2 on Fluorine-Doped Hierarchically Porous Carbon. *J. Catal.* **2018**, *357*, 118–126.

(41) Gao, J.; Liu, B. Progress of Electrochemical Hydrogen Peroxide Synthesis over Single Atom Catalysts. *ACS Mater. Lett.* **2020**, *2* (8), 1008–1024.

(42) Fortunato, G. V.; Pizzutilo, E.; Mingers, A. M.; Kasian, O.; Cherevko, S.; Cardoso, E. S. F.; Mayrhofer, K. J. J.; Maia, G.; Ledendecker, M. Impact of Palladium Loading and Interparticle Distance on the Selectivity for the Oxygen Reduction Reaction toward Hydrogen Peroxide. *J. Phys. Chem. C* **2018**, *122* (28), 15878–15885.

(43) Venarusso, L. B.; Boone, C. V; Bettini, J.; Maia, G. Carbon-Supported Metal Nanodendrites as Efficient, Stable Catalysts for the Oxygen Reduction Reaction. *J. Mater. Chem. A* **2018**, *6* (4), 1714–1726.

(44) Paulus, U. A.; Schmidt, T. J.; Gasteiger, H. A.; Behm, R. J. Oxygen Reduction on a High-Surface Area Pt/Vulcan Carbon Catalyst: A Thin-Film Rotating Ring-Disk Electrode Study. *J. Electroanal. Chem.* **2001**, *495* (2), 134–145.

(45) Antoine, O.; Durand, R. RRDE Study of Oxygen Reduction on Pt Nanoparticles inside Nafion®: H_2O_2 Production in PEMFC Cathode Conditions. *J. Appl. Electrochem.* **2000**, *30* (7), 839–844.

(46) De Lima, F.; Maia, G. Oxidized/Reduced Graphene Nanoribbons Facilitate Charge Transfer to the $Fe(CN)_6^{3-}/Fe(CN)_6^{4-}$ Redox Couple and towards Oxygen Reduction. *Nanoscale* **2015**, *7* (14), 6193–6207.

(47) Kou, R.; Shao, Y.; Wang, D.; Engelhard, M. H.; Kwak, J. H.; Wang, J.; Viswanathan, V. V.; Wang, C.; Lin, Y.; Wang, Y.; Aksay, I. A.; Liu, J. Enhanced Activity and Stability of Pt Catalysts on Functionalized Graphene Sheets for Electrocatalytic Oxygen Reduction. *Electrochem. commun.* **2009**, *11* (5), 954–957.

(48) Grzelczak, M.; Pérez-Juste, J.; Mulvaney, P.; Liz-Marzán, L. M. Shape Control in Gold Nanoparticle Synthesis. *Chem. Soc. Rev.* **2008**, *37* (9), 1783–1791.

(49) Boone, C. V.; Maia, G. Pt–Pd and Pt–Pd–(Cu or Fe or Co)/Graphene Nanoribbon Nanocomposites as Efficient Catalysts toward the Oxygen Reduction Reaction. *Electrochim. Acta* **2017**, *247*, 19–29.

(50) Venarusso, L. B.; Bettini, J.; Maia, G. Superior Catalysts for Oxygen Reduction Reaction Based on Porous Nanostars of a Pt, Pd, or Pt-Pd Alloy Shell Supported on a Gold Core. *ChemElectroChem* **2016**, *3* (5), 749–756.

(51) Tang, Q.; Shan, Z.; Wang, L.; Qin, X. MoO_2–Graphene Nanocomposite as Anode Material for Lithium-Ion Batteries. *Electrochim. Acta* **2012**, *79*, 148–153.

(52) Xiao, D.; Zhang, J.; Li, X.; Zhao, D.; Huang, H.; Huang, J.; Cao, D.; Li, Z.; Niu, C. Nanocarved MoS_2 –MoO_2 Hybrids Fabricated Using in Situ Grown MoS_2 as Nanomasks. *ACS Nano* **2016**, *10* (10), 9509–9515.

(53) Wang, L.; Yamauchi, Y. Block Copolymer Mediated Synthesis of Dendritic Platinum Nanoparticles. *J. Am. Chem. Soc.* **2009**, *131* (26), 9152–9153.

(54) Cardoso, E. S. F.; Fortunato, G. V.; Maia, G. Use of Rotating Ring-Disk Electrodes to Investigate Graphene Nanoribbon Loadings for the Oxygen Reduction Reaction in Alkaline Medium. *ChemElectroChem* **2018**, *5* (13), 1691–1701.

(55) Wang, Z.; Feng, J.; Li, X.; Oh, R.; Shi, D.; Akdim, O.; Xia, M.; Zhao, L.; Huang, X.; Zhang, G. Au-Pd Nanoparticles Immobilized on TiO_2 Nanosheet as an Active and Durable Catalyst for Solvent-Free Selective Oxidation of Benzyl Alcohol. *J. Colloid Interface Sci.* **2021**, *588*, 787–794.

(56) Rakočević, L.; Štrbac, S.; Srejić, I. Hydrogen Evolution on Au/GC and PdAu/GC Nanostructures in Acid Solution: AFM, XPS, and Electrochemical Study. *Int. J. Hydrogen*

Energy **2021**, *46* (13), 9052–9063.

(57) Sharpe, R.; Counsell, J.; Bowker, M. Pd Segregation to the Surface of Au on Pd(111) and on Pd/TiO_2 (110). *Surf. Sci.* **2017**, *656*, 60–65.

(58) Enache, D. I.; Edwards, J. K.; Landon, P.; Solsona-Espriu, B.; Carley, A. F.; Herzing, A. A.; Watanabe, M.; Kiely, C. J.; Knight, D. W.; Hutchings, G. J. Solvent-Free Oxidation of Primary Alcohols to Aldehydes Using Au-Pd/TiO_2 Catalysts. *Science (80-.).* **2006**, *311* (5759), 362–365.

(59) Xu, J.; White, T.; Li, P.; He, C.; Yu, J.; Yuan, W.; Han, Y.-F. Biphasic Pd−Au Alloy Catalyst for Low-Temperature CO Oxidation. *J. Am. Chem. Soc.* **2010**, *132* (30), 10398–10406.

(60) Hayashi, N.; Sakai, Y.; Tsunoyama, H.; Nakajima, A. Development of Ultrafine Multichannel Microfluidic Mixer for Synthesis of Bimetallic Nanoclusters: Catalytic Application of Highly Monodisperse AuPd Nanoclusters Stabilized by Poly(N-Vinylpyrrolidone). *Langmuir* **2014**, *30* (34), 10539–10547.

(61) Lopez-Sanchez, J. A.; Dimitratos, N.; Hammond, C.; Brett, G. L.; Kesavan, L.; White, S.; Miedziak, P.; Tiruvalam, R.; Jenkins, R. L.; Carley, A. F.; Knight, D.; Kiely, C. J.; Hutchings, G. J. Facile Removal of Stabilizer-Ligands from Supported Gold Nanoparticles. *Nat. Chem.* **2011**, *3* (7), 551–556.

(62) Militello, M. C.; Simko, S. J. Palladium Chloride ($PdCl_2$) by XPS. *Surf. Sci. Spectra* **1994**, *3* (4), 402–409.

(63) Li, Z.; Gao, F.; Furlong, O.; Tysoe, W. T. Adsorption of Carbon Monoxide Au/Pd(100) Alloys in Ultrahigh Vacuum: Identification of Adsorption Sites. *Surf. Sci.* **2010**, *604* (2), 136–143.

(64) Boone, C. V.; Maia, G. Lowering Metal Loadings onto Pt–Pd–Cu/Graphene Nanoribbon Nanocomposites Affects Electrode Collection Efficiency and Oxygen Reduction Reaction Performance. *Electrochim. Acta* **2019**, *303*, 192–203.

(65) Fortunato, G. V.; Cardoso, E. S. F.; Martini, B. K.; Maia, G. Ti/Pt−Pd-Based Nanocomposite: Effects of Metal Oxides on the Oxygen Reduction Reaction. *ChemElectroChem* **2020**, *7* (7), 1610–1618.

(66) Bard, A. J.; Parsons, R.; Jordan, J. *Standard Potentials in Aqueous Solution*, 1st ed.; CRC Press, 1985.

(67) Ham, H. C.; Hwang, G. S.; Han, J.; Nam, S. W.; Lim, T. H. On the Role of Pd Ensembles in Selective H_2O_2 Formation on PdAu Alloys. *J. Phys. Chem. C* **2009**, *113* (30), 12943–12945.

(68) Ham, H. C.; Hwang, G. S.; Han, J.; Yoon, S. P.; Nam, S. W.; Lim, T. H. Importance of Pd Monomer Pairs in Enhancing the Oxygen Reduction Reaction Activity of the AuPd(1 0 0) Surface: A First Principles Study. *Catal. Today* **2016**, *263*, 11–15.

(69) Staszak-Jirkovský, J.; Ahlberg, E.; Panas, I.; Schiffrin, D. J. The Bifurcation Point of the Oxygen Reduction Reaction on Au–Pd Nanoalloys. *Faraday Discuss.* **2016**, *188*, 257–278.

(70) Jirkovsk, J. S.; Panas, I.; Ahlberg, E.; Halasa, M.; Romani, S.; Schi, D. J. Single Atom Hot-Spots at Au À Pd Nanoalloys for Electrocatalytic H2O2 Production. *J. Am. Chem. Soc* **2011**, 19432–19441.

(71) Jirkovský, J. S.; Panas, I.; Romani, S.; Ahlberg, E.; Schiffrin, D. J. Potential-Dependent Structural Memory Effects in Au-Pd Nanoalloys. *J. Phys. Chem. Lett.* **2012**, *3* (3), 315–321.

(72) Devivaraprasad, R.; Nalajala, N.; Bera, B.; Neergat, M. Electrocatalysis of Oxygen Reduction Reaction on Shape-Controlled Pt and Pd Nanoparticles—Importance of Surface Cleanliness and Reconstruction. *Front. Chem.* **2019**, *7*.

(73) Zhao, X.; Liu, Y. Origin of Selective Production of Hydrogen Peroxide by Electrochemical Oxygen Reduction. *J. Am. Chem. Soc.* **2021**, *143* (25), 9423–9428.

(74) Fortunato, G. V.; Kronka, M. S.; dos Santos, A. J.; Ledendecker, M.; Lanza, M. R. V. Low Pd Loadings onto Printex L6: Synthesis, Characterization and Performance towards H_2O_2 Generation for Electrochemical Water Treatment Technologies. *Chemosphere* **2020**, *259*, 127523.

(75) Zhou, W.; Li, M.; Ding, O. L.; Chan, S. H.; Zhang, L.; Xue, Y. Pd Particle Size Effects on

Oxygen Electrochemical Reduction. *Int. J. Hydrogen Energy* **2014**, *39* (12), 6433–6442.

(76) Yano, H.; Inukai, J.; Uchida, H.; Watanabe, M.; Babu, P. K.; Kobayashi, T.; Chung, J. H.; Oldfield, E.; Wieckowski, A. Particle-Size Effect of Nanoscale Platinum Catalysts in Oxygen Reduction Reaction: An Electrochemical and 195Pt EC-NMR Study. *Phys. Chem. Chem. Phys.* **2006**, *8* (42), 4932.

(77) Park, Y. C.; Tokiwa, H.; Kakinuma, K.; Watanabe, M.; Uchida, M. Effects of Carbon Supports on Pt Distribution, Ionomer Coverage and Cathode Performance for Polymer Electrolyte Fuel Cells. *J. Power Sources* **2016**, *315*, 179–191.

(78) Yoo, S. J.; Jeon, T.-Y.; Lee, K.-S.; Park, K.-W.; Sung, Y.-E. Effects of Particle Size on Surface Electronic and Electrocatalytic Properties of Pt/TiO_2 Nanocatalysts. *Chem. Commun.* **2010**, *46* (5), 794–796.

(79) Zhao, X.; Zhu, J.; Liang, L.; Liao, J.; Liu, C.; Xing, W. Enhanced Activity of Pt Nano-Crystals Supported on a Novel TiO_2@N-Doped C Nano-Composite for Methanol Oxidation Reaction. *J. Mater. Chem.* **2012**, *22* (37), 19718–19725.

(80) Pourbaix, M. *Atlas of Electrochemical Equilibria in Aqueous Solutions*, 2nd ed.; Nat. Assoc. of Corrosion Engineers: Houston, 1974.

(81) Saji, V. S.; Lee, C. W. Molybdenum, Molybdenum Oxides, and Their Electrochemistry. *ChemSusChem* **2012**, *5* (7), 1146–1161.

(82) Chen, X.; Granda-Marulanda, L. P.; McCrum, I. T.; Koper, M. T. M. Adsorption Processes on a Pd Monolayer-Modified Pt(111) Electrode. *Chem. Sci.* **2020**, *11* (6), 1703–1713.

(83) Attard, G. A.; Bannister, A. The Electrochemical Behaviour of Irreversibly Adsorbed Palladium on Pt(111) in Acid Media. *J. Electroanal. Chem. Interfacial Electrochem.* **1991**, *300* (1–2), 467–485.

(84) Nishikawa, H.; Yano, H.; Inukai, J.; Tryk, D. A.; Iiyama, A.; Uchida, H. Effects of Sulfate on the Oxygen Reduction Reaction Activity on Stabilized Pt Skin/PtCo Alloy Catalysts from 30 to 80 °C. *Langmuir* **2018**, *34* (45), 13558–13564.

(85) Climent, V.; Marković, N. M.; Ross, P. N. Kinetics of Oxygen Reduction on an Epitaxial Film of Palladium on Pt(111) † , ‡. *J. Phys. Chem. B* **2000**, *104* (14), 3116–3120.

(86) Shao, M.; Odell, J.; Humbert, M.; Yu, T.; Xia, Y. Electrocatalysis on Shape-Controlled Palladium Nanocrystals: Oxygen Reduction Reaction and Formic Acid Oxidation. *J. Phys. Chem. C* **2013**, *117* (8), 4172–4180.

Graphical Abstract